1 Vehicle induced turbulence and atmospheric pollution

2 Paul A. Makar[1], Craig Stroud[1], Ayodeji Akingunola[1], Junhua Zhang[1], Shuzhan Ren[1], Philip Cheung[1],
3 Qiong Zheng[1]

4 [1]Air Quality Modelling and Integration Section, Air Quality Research Division, Atmospheric Science and Technology
5 Directorate, Environment and Climate Change Canada, 4905 Dufferin Street, Toronto, Ontario, M3H 5T4, Canada

6 *Correspondence to*: Paul A. Makar (paul.makar@canada.ca)

7 **Abstract.** Theoretical models of the Earth's atmosphere adhere to an underlying concept of flow driven by radiative transfer
8 and the nature of the surface over which the flow is taking place: heat from the sun and/or anthropogenic sources are the sole
9 sources of energy driving atmospheric constituent transport. However, another source of energy is prevalent in the human
10 environment at the very local scale – the transfer of kinetic energy from moving vehicles to the atmosphere. We show that
11 this source of energy, due to being co-located with combustion emissions, can influence their vertical distribution to the extent
12 of having a significant influence on lower troposphere pollutant concentrations throughout North America. The effect of
13 vehicle-induced turbulence on freshly emitted chemicals remains notable even when taking into account more complex urban
14 radiative transfer-driven turbulence theories at high resolution. We have designed a parameterization to account for the at-
15 source vertical transport of freshly emitted pollutants from mobile emissions resulting from vehicle-induced turbulence, in
16 analogy to sub-grid-scale parameterizations for plume rise emissions from large stacks. This parameterization allows vehicle-
17 induced turbulence to be represented at the scales inherent 3D chemical transport models, allowing its impact over large regions
18 to be represented, without the need for the computational resources and much higher resolution of large eddy simulation
19 models. Including this sub-grid-scale parameterization for the vertical transport of emitted pollutants due to vehicle-induced
20 turbulence into a 3D chemical transport model of the atmosphere reduces pre-existing North American nitrogen dioxide biases
21 by a factor of eight, and improves most model performance scores for nitrogen dioxide, particulate matter and ozone (for
22 example, reductions in root mean square errors of 20, 9 and 0.5 percent, respectively).

23 1 Introduction

24 A common and ongoing problem with theoretical descriptions of the Earth's atmosphere is a dichotomy in the representation
25 of turbulent transport, between the turbulence estimated in weather forecast models, and the turbulence required for accurate
26 simulations in air-quality forecast models. Representations of atmospheric turbulence used in weather forecast and climate
27 models have focused on parameterizations of "sub-gridscale turbulence"; descriptions of the storage and release of energy
28 derived from incoming solar radiation and anthropogenic heat release, physical factors in the built-environment, and the
29 transfer of sensible and latent heat between the built environment and the atmosphere. These efforts adhere to an underlying
30 concept of radiative-driven flow: heat transfer from the sun and/or anthropogenic sources being the source of energy behind

31 atmospheric motions. There has been considerable research focused on improving understanding radiative-driven flow in

32 urban areas (e.g. the advection and diffusion associated with buildings and street canyons (Mensink *et al.*, 2014), urban heat

33 island radiative transfer theory (Mason *et al.*, 2000), and in efforts to increase 3D model vertical and horizontal resolution in

34 order to better capture the physical environment (Leroyer et al, 2014). However, when these physical models of turbulence

35 are applied to problems involving the emissions, transport and chemistry of atmospheric pollutants, predicted surface

36 concentrations of emitted pollutants may be biased high, and concentrations aloft biased low, indicating the presence of missing

37 additional sources of atmospheric dispersion (Makar *et al.*, 2014; Kim *et al.*, 2015). Despite ongoing work to improve the

38 turbulence schemes in meteorological models (Makar *et al.*, 2014; Hu *et al.*, 2013; Klein *et al.*, 2014), computational predictive

39 models of atmospheric pollution typically make use of a constant "floor" or "cut-off" in the thermal turbulent transfer

40 coefficients provided by weather forecast models, sometimes with higher values of this cutoff over urban compared to rural

41 areas (Makar *et al.*, 2014), in an attempt to compensate for apparent insufficient vertical mixing of chemical tracers. The

42 turbulent mixing in these physical descriptions, while capable of reproducing observed meteorological conditions, do not

43 explain lower concentration observations of emitted atmospheric pollutants.

44 Large stack sources of pollutants provide a useful analogy in investigating the cause of this discrepancy. Emissions from these

45 sources occur at high temperatures, lofting their emitted mass high into the atmosphere as a result of buoyancy effects.

46 However, the physical size of the stacks (< 10 m diameter) is much smaller than the grid cell size used in regional models (km

47 to 10's of km). In order to capture the rapid vertical redistribution of emissions from large stacks, sub-grid-scale

48 parameterizations are used, in which buoyancy calculations are performed to determine plume heights, which are then used to

49 determine the distribution of freshly emitted pollutants (Briggs, 1975; Briggs, 1984; Gordon *et al.*, 2018; Akingunola *et al.*,

50 2018). For large stack emissions, these parameterizations account for the effect of the addition of energy (the hot exhaust gas)

51 on the local distribution of pollutants, and are essential in estimating initial vertical distribution of those pollutants.

52 In this work, we investigate the potential for another type of at-source energy to influence the vertical distribution of freshly

53 emitted pollutant concentrations: the addition of kinetic energy due to the displacement of air during the passage of vehicles

54 on roadways. Roadway observations in the 1970's showed that this transferred energy has a significant influence on the

55 transport of primary pollutants released from vehicle exhaust, with vehicle passage being associated with "a distinct bulge in

56 the high frequency range of the wind spectrum", "corresponding to eddy sizes on the order of a few metres" (Rao *et al.*, 1979).

57 The same work found that the variation in the concentration of non-reactive tracers could be attributed to wakes behind moving

58 vehicles. Subsequent theoretical development led to the creation of the roadway-scale models describing turbulence within a

59 few 10's of metres around and above roadways, in turn used to estimate the very local-level impact of vehicles on emitted

60 pollutant concentrations (Eskridge and Catalano, 1987). These models showed that near-roadway concentrations of emitted

61 pollutants were highly dependent on vehicle speed, with over a factor of two reduction in emission-normalized pollutant

62 concentrations being associated with an increase in vehicle speed from 20 to 100 km/hr (Eskridge *et al.*, 1991). With the

63 advent of portable, very high time resolution 3-D sonic anemometers, the turbulent kinetic energy of individual vehicles could

64 be measured directly, either aboard an instrumented trailer towed behind a vehicle11, or through instrumentation mounted

65 aboard a laboratory following other vehicles in traffic (Gordon *et al.*, 2012; Miller *et al.*, 2018).   However, the application of

66 this information has been limited up to now to theoretical and computational models of the near-roadway environment.

67 Regional air-quality models also have vertical resolution in the 10's of metres near the surface, suggesting the potential for

68 vehicle-induced turbulence (VIT) to influence turbulent mixing out of the lowest model layer(s).   Here we demonstrate that

69 this sub-grid-scale vertical transport process, which due to its highly localized spatial nature (over roadways), has a

70 disproportionate impact on the vertical distribution and transport of freshly emitted chemical tracers.   A comparable sub-grid-

71 scale process which has a similar influence on pollutants are the emissions from large stacks (Gordon *et al.*, 2018; Akingunola

72 *et al.*, 2018).   Accurate estimation of pollutant concentrations from the latter sources must take into account the at-source

73 buoyancy and exit velocity of high-temperature exhaust to determine the vertical distribution of fresh emissions.   Similarly,

74 our work focusses on determining the local lofting of pollutants from and due to moving vehicles, in order to adequately

75 represent the at-source vertical distribution of their emissions, on the larger scale.

76 The extent of the vertical influence of VIT varies depending on the configuration of vehicles on the roadway.   From

77 observations taken from a trailer following an isolated passenger van (Rao *et al.*, 2002), and large eddy simulation (LES) /

78 computational fluid dynamics (CFD) models of individual vehicles (Kim *et al.*, 2011; Kim *et al.*, 2016), the vertical distance

79 over which VIT can be distinguished from the background for isolated, *individual* vehicles (i.e. the mixing length) is on the

80 order of 2.5 to 5.13 m.   However, as we show in Methods and Results, for observations of *ensembles* of vehicles in traffic

81 (Gordon *et al.*, 2012; Miller *et al.*, 2018), and large eddy / computational fluid dynamics simulations of *ensembles* of vehicles

82 (Kim *et al.*, 2016; Woodward *et al.*, 2019; Zhang *et al.*, 2017), the mixing lengths associated with VIT are larger, on the order

83 of 10's of m, to as much as 41 m.   The vertical extent of the impacts of alternating low and high areas of surface roughness

84 have been shown to create downwind internal boundary layers to even more significant heights in the atmosphere (e.g 300m,

85 Bou-Zeid *et al.*, 2004, Figure 12), suggesting that impacts into the lower boundary layer due to the alternating roughness

86 elements (in our case, vehicles versus roadways) is not unreasonable.   We also show in Methods that the impact of VIT within

87 the context of an air-quality model is via changes to the vertical gradient of the thermal turbulent transfer coefficients; the

88 gradient of the sum of the natural turbulence and VIT terms, allows VIT to influence vertical mixing, even when model vertical

89 resolution is relatively coarse.

90 Large eddy simulation (LES) / computational fluid dynamics (CFD) models have shown the importance of VIT towards

91 modifying local values of turbulent kinetic energy, as noted in the references above.   However, these models require very small

92 grid cell sizes and time steps to allow forward time stepping predictions of future meteorology and chemistry.   These

93 constraints in turn severely limit the size of the domain in which they can be applied, and the processing time for simulations

94 for these reduced domains can be very high. For example, the FLUENT model was used by Kim et al (2016) with an adaptive

95 mesh with a minimum cell size of 1 cm, with a 100x20x20m domain, while Woodward et al (2019)'s implementation of

96 FLUENT had an equivalent cell size of 50 cm, operating in a domain of 600,000 nodes (a volume of 75,000 cubic metres),

97 and an adaptive timestep limited by a Courant number of 5.   The latter criteria implies a computation timestep of less than 0.09

98 s for a 100 km hr^{-1} vehicle (or wind) speed, while a 1 cm grid cell size implies a computation timestep of less than 1.8×10^{-3} s

99   timestep. Similarly, the LES model employed by Zhang et al (2017) utilized a 1m x 2m x 1m cell size and a computation

100   timestep of 0.03 s. In contrast, a 3D regional chemical transport model typically operates over a domain with may be

101   continental in extent, with limiting horizontal resolution on the order of kilometres, a limiting vertical resolution on the order

102   of 10's of metres, and timesteps on the order of 1 minute. These limits for regional chemical transport models are a function

103   of the need to provide chemical forecasts over a relatively large region, within a reasonable amount of current supercomputer

104   processing time. However, a "scale gap" exists between LES and regional chemical transport models – for regional chemical

105   transport models, parameterizations of the physical processes resolvable at the very high resolution of LES models are required.

106   In return, these parameterizations allow the relative impact of the parameterized processes on the urban to regional to

107   continental scales regional chemical transport models to be determined.

108   Here we make use of both the observational and LES modelling studies to devise a parameterization for VIT, which we then

109   apply at two different configurations of a regional chemical transport model (GEM-MACH). We show that VIT has a

110   potentially significant impact on pollutant concentrations at the urban, regional, and continental scales. Reductions of model

111   biases are of particular interest from the standpoint of the use of air-quality model predictions to determine chronic health

112   outcomes. The inclusion of VIT reduces the positive bias in predictions of North American and urban scale nitrogen dioxide

113   by factors of 8 and 2.6 respectively, and improves the accuracy of model simulations for most statistics for nitrogen dioxide,

114   ozone and particulate matter.

115   **2 Methodology**

116   **2.1 Theoretical development**

117   In contrast to the very local resolution "roadway" models used to examine the impact of vehicle motion on pollutant

118   concentration (Eskridge and Catalano, 1987; Eskridge *et al.*, 1991), and computational fluid dynamics modelling of vehicle

119   turbulence (Kim *et al.*, 2011; Kim *et al.*, 2016; Woodward *et al.*, 2019; Zhang *et al.*, 2017), 3D models of atmospheric pollution

120   (Galmarini *et al.*, 2015) have horizontal grid-cell sizes of a one to 10's of km, and thus emissions and vertical transport

121   associated with roadways must be approached from the standpoint of sub-grid-scale parameterizations. Measurements of the

122   turbulent kinetic energy (TKE) associated with vehicles are usually available on a "per-vehicle" or "per-vehicle within an

123   ensemble" basis. These observations provide the average on-road TKE per vehicle passing a point per unit time (Gordon *et*

124   *al.*, 2012; Miller *et al.*, 2018) and/or the shape of the enhanced TKE cross-section in the plane perpendicular to the vehicle's

125   motion (Rao *et al.*, 2002). A sub-gridscale parameterization linking these scales is therefore necessary in order to study the

126   impacts of VIT on the vertical redistribution of freshly emitted pollutants, and hence on large-scale atmospheric chemistry and

127   transport. Sub-gridscale parameterizations are commonly used in atmospheric models of weather forecasting to provide the

128   rates of change of processes which occur at scales smaller than the model's horizontal and/or vertical resolution: cloud

129   formation and buoyant plume rise from large stacks being a common example for model grid cell sizes of 10km or more (Kain,

130   2004; Briggs, 1975; Briggs 1984; Gordon *et al.*, 2018; Akingunola *et al.*, 2018).

131   Three separate problems must be addressed in the construction of such a VIT parameterization for atmospheric chemical

132   transport models, specifically:

133   (1)   What is the relationship governing the decrease in VIT with increasing distance (height) from the vehicles?

134   (2)   How can observation data, in units of vehicles per unit time, be related to variables more commonly available for

135   regional chemical transport models?

136   (3)   How can VIT be incorporated into a regional model in a manner that only the emissions due to vehicles are affected,

137   given that the vehicle-induced turbulence will have the most significant impact on emissions from moving vehicles due to the

138   relatively low area fraction of roadway area within a given grid cell?

139   We address each of these issues in the sub-sections that follow.

140   **2.2 Changes in VIT with Height**

141   Measurements of TKE behind a passenger van (Rao *et al.*, 2002) typically show a smooth distribution, with TKE decreasing

142   both above and below the height of the upper trailing edge of the moving vehicle. Similar results have been seen from very

143   high resolution computational fluid dynamics modelling of the flow around individual vehicles, though the shape of the vehicle

144   and the arrangement of vehicles on the roadway can have a strong influence on the location of the maximum and shape of the

145   vertical profile in TKE (Kim *et al.*, 2011; Kim *et al.*, 2016). We examined four datasets (Rao *et al.*, 2002; Kim *et al.*, 2016;

146   Woodward *et al.*, 2019; Zhang *et al.*, 2017) to evaluate the extent to which a Gaussian distribution may be used to represent

147   the decrease in VIT with height above moving vehicles, as well as examining the expected range of mixing lengths which may

148   result from VIT. A Gaussian distribution of TKE with height is given by equation (1), where $I_q(z)$ is the time integrated added

149   TKE value for vehicle type q with height z (m^{2}s^{-1}), h_q is the height of the vehicle, and A_q and σ_q are numerical constants:

150
$$I_q(z) = \frac{A_q}{\sqrt{2\,\pi\,\sigma_q^2}} e^{\left(-\frac{(z-h_q)^2}{2\,\sigma_q^2}\right)} \tag{1}$$

151   Equation (1) may be re-written as:

152
$$ln\left(\sqrt{2\,\pi}I_q(z)\right) = ln\left(\frac{A_q}{\sigma_q}\right) - \frac{(z-h_q)^2}{2\,\sigma_q^2} \tag{2}$$

153   Equation (2) shows that values of $-\left(z-h_q\right)^2$ versus $ln\left(\sqrt{2\,\pi}I_q(z)\right)$, with the values of z taken from vertical profiles of $I_q(z)$

154   in the literature, will yield a slope of $\frac{1}{2\,\sigma_q^2}$ and an intercept of $ln\left(\frac{A_q}{\sigma_q}\right)$, and the correlation coefficient for this relationship may

155   be used to judge the accuracy of the use of a Gaussian distribution to describe the decrease in TKE with height above moving

156   vehicles. The resulting relationships may also be used to describe the vertical mixing length, defined "as the diameter of the

157   masses of fluid moving as a whole in each individual case; or again, as the distance traversed by a mass of this type before it

158   becomes blended in with neighbouring masses" (Prandtl, 1925; Bradshaw, 1974). Here we assume that this blending has

159 occurred at the height at which the Gaussian has dropped to 0.01 of the value at $z=h_q$ (i.e. the value of z at which VIT has

160 reached 1% of its maximum value (i.e. $e^{\left(-\frac{(z-h_q)^2}{2\,\sigma_q^2}\right)} = 0.01$).

161 An example of the analysis used to construct Table 1 appears below (Figure 1), for a CFD example for an ensemble of vehicles,

162 taken from the literature (Kim *et al.*, 2016). In this figure, contours of TKE are shown as solid lines. TKE values as a function

163 of height at three locations behind the trucks were used to determine σ_q and hence estimate the length scale via equations (1)

164 and (2). A notable feature of this example is the substantial increase in length scale which occurs between the initial vehicle

165 (a transport truck) and subsequent downwind vehicles (compare height of TKE contours, and the resulting length scales in

166 Figure 1, between left and right sides of the figure). Increases in downwind turbulent length scales associated with vehicles

167 moving in close ensembles are a common feature in the literature.

168

169 This analysis (see Table 1) shows that a Gaussian distribution accounts for much of the variability in TKE with height

170 (correlation coefficients of 0.54 to 0.99), and under realistic traffic conditions, the mixing lengths increase in size, and may be

171 considerably larger than those of isolated vehicles.

172 Two VIT mobile laboratory studies (Gordon *et al.*, 2012; Miller *et al.*, 2018) observed vehicle-per-second TKE for vehicles

173 moving in ensembles along multilane roadways, aggregated by vehicle classes using the same methodology, to derive formulae

174 for the net TKE added by VIT at 4m and 2m (the height of the instrumentation used in these studies). We combine these data

175 here to determine the change in VIT with height. Setting E as the TKE added due to the vehicles, two formulae result:

176
$$E(4m) = 1.8\,F_c + 2.2\,F_m + 20.4\,F_t$$
$$E(2m) = 2.4\,F_c + 6.2\,F_m + 14.8\,F_t \tag{3}$$

177 Where *E(4m)* and *E(2m)* are the TKE added driving within the ensemble at 4 and 2 m elevation from these two studies (m^2 s^{-2}

178), and F_c, F_m, and F_t are the number of passenger cars, mid-sized (vans, flatbed pickup trucks, and SUVs) and large vehicles

179 (10 to 18 wheel heavy-duty vehicles) travelling past a given point on the highway per second. The numerical coefficients are

180 the time integrated TKE values (I_q) at the two heights (m^{2}s^{-1}). An alternative approach would be to make use of vehicle speed

181 data within each grid cell and parameterizations utilizing vehicle speed (Di Sabatino *et al.*, 2003; Kastner-Klein *et al.*, 2003)

182 to construct TKE additions due to the sub-grid-scale roadways. However, vehicle speed information is not currently readily

183 available on a gridded hourly basis, while estimates of vehicle km travelled are available in gridded form due to their use in

184 emissions processing, and making the simple scaling assumption that the vehicles travel across one dimension of a grid cell

185 allows us to generate the F_c values required to estimate TKE. Note that vehicle speed is implicit in this methodology utilizing

186 VKT – higher speeds will result in a greater number of vehicle km travelled per unit time, and hence higher TKE values. As

187 in the above discussion, we assume a Gaussian distribution of the coefficients of the TKE equations of (3) with height for each

188 vehicle, where $h_q = 1.5$m, 1.9m and 4.11m for cars, mid-sized vehicles and trucks, respectively, with each of the 2m and 4m

189 values of the coefficients of (3) being used to determine the corresponding values of A_q and σ_q of equation (1), (i.e. $q = c,m,t$).

190 The resulting height-dependent formulae may be used to replace the coefficients of (3), leading to the following formula for

191 the net turbulent kinetic energy associated with the number of vehicles in transit along a given stretch of roadway at a given

192 time:

$$
\begin{aligned}
E_{net}(z) = \ & 2.43 F_c e^{[-2.40 x 10^{-2}(z-1.5)^2]} \\
& + 15.58 F_m e^{[-1.18 x 10^{-1}(z-1.9)^2]} \\
& + 20.43 F_t \, e^{[-3.61 x 10^{-2}(z-4.11)^2]}
\end{aligned}
\tag{4}
$$

194 Most 3-D chemical transport models make use of some variation of "K-theory" diffusion to link turbulent kinetic energy to

195 mixing, with the vertical mixing of a transported variable c due to turbulence at heights z being related to the thermal turbulent

196 transfer coefficient K via:

$$
\frac{\partial c}{\partial t} = \frac{\partial}{\partial z}\left(K \frac{\partial c}{\partial z} \right)
\tag{5}
$$

198 Finite differences and tridiagonal matrix solvers are usually used to forward integrate equation (5). For example, the solver

199 used in the GEM-MACH model uses the following finite difference for the spatial derivatives (both spatial derivatives are

200 $O(\Delta\sigma^2)$, the derivatives are carried out in, and the K values are transformed into, $\sigma = \frac{P}{P_0}$ coordinates as $\tilde{K}$, where P is the

201 pressure, and P_0 is the surface pressure):

$$
\frac{c_i^{n+1}-c_i^n}{\Delta t} = \frac{\frac{1}{2}(\tilde{K}_{i+1}+\tilde{K}_i)\left(\frac{c_{i+1}-c_i}{\sigma_{i+1}-\sigma_i}\right) - \frac{1}{2}(\tilde{K}_i+\tilde{K}_{i-1})\left(\frac{c_i-c_{i-1}}{\sigma_i-\sigma_{i-1}}\right)}{\sigma_{i+\frac{1}{2}}-\sigma_{i-\frac{1}{2}}}
\tag{6}
$$

203 Note in (6) that the prognostic values of K calculated by the weather forecast model are on the same vertical levels as

204 concentration; values of the additional component of K associated with VIT must therefore be calculated for model layers as

205 opposed to layer interfaces.

206 K and E may be linked through the relationship of Prandtl, where l is a characteristic length scale:

$$
K = 0.4 \, l\sqrt{E}
\tag{7}
$$

208 As was done for Table 1, we have chosen this value on a per-vehicle basis as the vertical location at which the Gaussian

209 profiles derived above reach 0.01 (i.e. 1%) of their maximum value. Using each of the coefficient values of (3) at the two

210 heights, in conjunction with equation (1) treated as a two-variable in two unknowns (A_q, σ_q) problem we find values of l_c, l_m,

211 and l_t of 13.56, 6.25, and 11.28 m, respectively. These values are based on observed traffic conditions, and fall well within

212 the range of mixing lengths provided for vehicle ensembles in Table 1, however, we note that they are a source of uncertainty,

213 with the percent uncertainties (Gordon *et al.*, 2012) associated with the 4m values at ±52%, ±157%, and ±12% for cars, mid-

214 sized vehicles and trucks, respectively. The relatively low values of l_m and high uncertainties in the corresponding mid-sized

215 vehicle per-vehicle estimates of TKE relative to the other vehicle types are likely the result of a combination of small sample

216 size (Gordon *et al.* (2012) noted the relative proportion of the three vehicle classes as 89.9% cars, 4.8% mid-sized, and 5.3%

217 trucks, respectively) and the variety of ensemble versus isolated vehicles sampled (noting the variation in Table 1 for vehicles

218 within the smaller vehicle size classes). Additional observations of vehicle turbulence are clearly needed, particularly in the

219 region above the largest vehicles on the road (4.1m), using remote sensing techniques such as Doppler lidar, in order to improve

220 mixing length estimates. However, the values used here are reasonable with respect to the available data, and while likely

221 overestimating the mixing length associated with isolated vehicles (Rao *et al.*, 2002; Kim *et al.*, 2016) likely underestimate

222 the mixing length of ensembles of vehicles (Kim *et al.*, 2016), particularly for ensembles moving within street canyons

223 (Woodward *et al.*, 2019; Zhang *et al.*, 2017). The latter represent the some of the specific regions where vehicle emissions are

224 likely to dominate.

225 We derive the following formula for the addition to the thermal turbulent transfer coefficient associated with vehicle passage

226 as a function of height:

227
$$K_{VIT}(z) = 0.4 \, \frac{l_c F_c + l_m F_m + l_t F_t}{F_c + F_m + F_t} \sqrt{\begin{pmatrix} 2.43 F_c e^{[-2.40 x 10^{-2}(z-1.5)^2]} \\ +15.58 F_m e^{[-1.18 x 10^{-1}(z-1.9)^2]} \\ +20.43 F_t e^{[-3.61 x 10^{-2}(z-4.11)^2]} \end{pmatrix}} \qquad (8)$$

228

229 The use of (8) must be undertaken with care. Like most regional air-quality models, the vertical resolution of GEM-MACH

230 used here is relatively coarse (the first four model layer midpoints are located approximately 24.9, 99.8, 205.0, and 327.0 m

231 above the surface). Layer midpoint values must be representative of the layer resolution in order to describe the impact of

232 VIT on the layer. A simple linear interpolation between the peak values of K_{VIT} and the first model interface will overestimate

233 the impact of VIT within the lowest model layer, while the use of (8) for the mid-point value alone will underestimate the

234 influence of VIT within the lowest part of the first model layer. The best representation of a sub-grid-scale scalar quantity

235 within a discrete model layer is its vertical average within that layer. Here, we calculate the vertically integrated average of

236 (8) within each model layer, to provide the best estimate of the impact of VIT, to within the vertical resolution of the model.

237 **2.3 VIT and Model Vertical Resolution**

238 The issue of the vertical extent of the impact of VIT is worth considering in the context of model layer thickness. Given that

239 the vertical length scale of added VIT is on the order of 10's of metres, as denoted in the studies quoted herein, it is reasonable

240 to question whether the added turbulence should be expected to have an impact on the dispersion of pollutants. This apparent

241 contradiction is easily resolved by noting, (1) that the turbulence due to VIT is added as an addition to the pre-existing

242 "meteorological" thermal turbulent transfer coefficient (with the *net* turbulence profile, not the VIT alone, determining its

243 impact on vertical mixing); and (2) that the impact of this net turbulence does not depend just on the magnitude of the net

244 coefficients of thermal turbulent transfer, but also on their vertical gradient. This second point can be illustrated by expanding

245 the diffusion equation using the chain run of calculus (i.e. $\frac{\partial c}{\partial t} = \frac{\partial}{\partial z}\left(K_{net}\frac{\partial c}{\partial z}\right) = K_{net}\frac{\partial^2 c}{\partial z^2} + \frac{\partial K_{net}}{\partial z}\frac{\partial c}{\partial z}$), and the aid of an example,

246 shown in Figure 2. Figure 2 displays examples of cases where the concentration gradient and natural thermal turbulent transfer

247 coefficient both decrease linearly with height (Figure 2(a,b)), and where the concentration gradient decreases with height while

248 the natural thermal turbulent transfer coefficients increase with height (Figure 2(c,d)). The added K_{VIT} is shown as a blue

249 dashed line, and the net vertical thermal turbulent transfer is shown as a red line. Figure 2 (a) and Figure 2(c) depict these

250 curves at a high vertical resolution, while Figure 2(b) and Figure 2(d) depict them at a low (regional model) resolution. Note

251   that in the latter, the vehicle-induced addition to the net thermal turbulent transfer coefficient depicted in Figure 2(a,c) lies

252   entirely within the lowest model layer of Figure 2(b,d). In both Figure 2(a) and Figure 2(b), the impact of K_{VIT} is to slow the

253   build-up of near-surface concentrations. In both Figure 2(c) and Figure 2(d), the impact of K_{VIT} is to more rapidly vent near-

254   surface concentrations further up into the atmosphere. That is, at both high and low resolution, K_{VIT} affects near-surface

255   concentrations, due to the vertical gradient of $\frac{\partial K_{net}}{\partial z}$). Centered difference calculations for the low resolution case are shown

256   in Figure 2(b,d) to illustrate the point that gradients in low vertical resolution net diffusivity result in reductions in lowest

257   model layer trapping, and increases in venting from this lowest layer. In both of these cases, the addition of vehicle turbulence

258   to the lowest model layer changes the gradient of the net thermal turbulent transfer coefficient, in turn leading to reduced

259   surface concentrations. The above example illustrates the manner in which VIT may have an impact even on relatively low

260   vertical model resolution.

261   **2.4 Relating VIT to Available Gridded Data – Vehicle Km Travelled**

262   Along individual roadways, the equation (8) makes use of F_c, F_m, and F_t observations at points along roadways within a grid-

263   cell, hence deriving local estimates of VIT. This data is currently difficult to obtain for large-scale applications, and hence

264   we have turned to secondary sources of information to estimate these three terms. Vehicle Kilometer Travelled (VKT) is used

265   for estimating onroad vehicle emissions at jurisdiction level (e.g. county level for the US and province level for Canada) for

266   the national emissions inventory. Emissions processing systems used for air-quality models make use of spatial surrogates to

267   help determine the spatial allocation of the mass emitted from different types of vehicles on different roadways (Adelman *et*

268   *al.*, 2017). The same set of surrogates is used for calculating VKT (km s^{-1}) for each grid cell of the model domain (varying

269   by hour of day and day of week, for each of the three vehicle categories listed (see Figure 3), in turn providing diurnal variations

270   of VIT matching traffic flow. The data shown are derived from 2006 Canadian (Taylor, 2019) and 2011-based projected 2017

271   US VKT (EPA, 2017). Note that for the 10km grid cell size used here, values of F_c, F_m, and F_t may be derived by dividing

272   these numbers by 10. The largest contribution to total vehicle km travelled is by the "cars" class (Figure 3(a)) due to their

273   greater numbers (the originating study (Miller *et al.*, 2018) found that 89.9% of vehicles measured were cars), followed by

274   trucks (Figure 3(c); 5.3% of vehicles measured), and mid-sized vehicles (Figure 3(b); 4.8% of vehicles measured).

275   These VKT data may be linked to the above VIT formula (8), provided the distance each vehicle is travelling within that grid

276   cell is known. Here, we have made two additional assumptions. The first assumption is that each vehicle carries out a simple

277   transit of the cell – the distance travelled is the cell-size. While this may be a reasonable first-order approximation, we note

278   that it has limitations: for example, when the number of vehicles on the roads overwhelm the capacity of the roads (rush-hour

279   traffic jams) the distance travelled decreases. However, under these circumstances the VKT values will also decrease; the

280   impact of rush-hour conditions should to some extent be included within the VKT estimates available for emissions processing

281   systems. The second assumption is that the VKT contributions within a grid-cell are additive – i.e. that their numbers may be

282   added via the "F" terms in (6) (Gordon *et al.*, 2012; Miller *et al.*, 2018), an assumption found to be accurate in CFD modelling

283 (Kim *et al.*, 2016). Note that this assumption may result in overestimates of the net TKE – a better methodology for future

284 work would be to collect and make use of statistics of vehicle density by roadway type within each grid-cell. However, we

285 note that assuming that vehicles are evenly distributed over roadways in a grid cell would result in a net underestimate of the

286 TKE contributed over the larger roadways and main arteries of urban areas.

287 Example 10 AM EDT North American 10km resolution gridded vehicle-induced thermal turbulent transfer coefficient values

288 (K_{VIT}, equation 8) created using these assumptions, and an example vertical profile of K_{VIT} for central Manhattan Island at

289 0.5m vertical resolution are shown in Figure 4. The resulting enhancements to "natural" K values at the vertical resolution of

290 the version of the GEM-MACH air-quality model, at 2.5km horizontal resolution, are shown in Figure S1 as dashed lines. The

291 enhancements are confined to the lowest model layer, as might be expected from the vertical resolution employed in this

292 version of GEM-MACH. Nevertheless, the values are sufficient to significantly change simulated vertical transport due to

293 modifications to the resolved gradient in thermal turbulent transfer coefficients, as discussed above. Both the magnitude and

294 gradient of $K_{net} = K + K_{VIT}$ may contribute to the concentration changes: breaking the vertical diffusion equation down using

295 the chain rule, (5) may be rewritten

$$\frac{\partial c}{\partial t} = K\frac{\partial^2 c}{\partial z^2} + \frac{\partial K}{\partial z}\frac{\partial c}{\partial z} \tag{9}$$

297 Both terms on the right-hand-side of (9) may contribute to decreases in concentration c at the surface and increases in

298 concentrations aloft. If the near-surface concentration profile ($\partial c/\partial z$) is negative (concentrations decrease with height), then

299 increases in K will result in surface concentration decreases). If this results in sufficient lofting that the concentration profile

300 maximizes above the ground (i.e. $\partial c/\partial z$ becomes positive near the surface), then decreasing values of K with height (i.e.

301 negative values of $\partial K/\partial z$) will also result in a shift towards negative rates of change, through the second term in the right-hand-

302 side of (9). All six panels of Figure S1 show increased *K* values; i.e. increases in the first term in (9). All six panels also

303 show a trend of $\partial K/\partial z$ becoming more negative, decreasing the magnitude of the second term in (9) in Figure S1 (b,c,d,f), and

304 switching to a negative rate of change in Figure S1(a,e). Both changes in the magnitude and gradient of *K* resulting from VIT

305 contribute to the resulting changes in surface concentration.

306 The thermal turbulent transfer coefficient values of Figure S1 may also be compared to the minima on "natural" K values

307 imposed in air pollution models in an attempt to account for missing subgrid-scale mixing (Makar *et al.*, 2014; these are

308 typically on the order of 0.1 to 2.0 m^2s^{-1}). Aside from Figure S1(a), the vertical profiles here would not be modified by these

309 lower limits. We also note that these VIT-induced changes in total thermal turbulent transfer coefficients only impact the

310 species emitted at the road-way level, as discussed below.

2.5 Construction of a Sub-Gridscale Parameterization for On-Road Vehicle-Induced Turbulence

312 We note that the portion of the area of a grid-cell which is roadway-covered will be relatively small for most air pollution

313 model resolutions, such as those considered here. For example, satellite imagery of the largest freeways show these to have

314 a width of less than 400m. Hence, the largest roads make up less than 1/5 of the total area of a 2.5km grid-cell, and less than

315   1/20 of a 10km grid cell). The largest impact of VIT is thus likely to be for the chemical species being emitted by the mobile

316   sources, in terms of the grid-cell average concentration. Furthermore, the grid cell approach common to these models results

317   in horizontal numerical diffusion from the roadway scale to the grid cell scale: sub-grid-cell scale emissions are automatically

318   mixed across the extent of the grid cell. The key impact of VIT will thus be in the vertical dispersion of the pollutants emitted

319   from mobile sources. We must therefore devise a numerical means to ensure this additional source of diffusion is added to the

320   model, bearing these constraints in mind.

321   Two examples of similar sub-gridscale processes appear in the literature. The first example are the cloud convection

322   parameterizations used in numerical weather forecast models (Kain *et al.*, 2004), wherein the formation and vertical transport

323   associated with convective clouds, are known to occur at smaller scales than the grid cell size employed in a numerical weather

324   prediction model, are treated using sub-gridscale parameterizations. In these parameterizations, cloud formation and transport

325   are calculated within the grid-cell on a statistical basis, using formulae linking the local processes to the resolvable scale of the

326   model. The second example is found in the treatment of emissions from large stacks within air-quality forecast models (Gordon

327   *et al.*, 2018; Akingunola *et al.*, 2018). These sources usually have stack diameters on the order less than 10m, and these sources

328   emit large amounts of pollutant mass at high temperatures and velocities. In order to represent these sources, the most common

329   approach is to calculate the height of the buoyant plume using the predicted ambient meteorology (vertical temperature profile,

330   etc.) as well as the stack parameters (exit velocity, exit temperature, stack diameter). The emitted mass during the model

331   timestep from the stack is then distributed over a defined vertical region within the gridcell in which the source resides. Note

332   that the mass is also automatically distributed immediately in the horizontal dimension within the grid cell – the key issue is

333   to ensure that the emitted mass is properly distributed in the vertical dimension. Our aim in the VIT parameterization that

334   follows is identical in intent to that of the existing major point source treatments in air-quality models: to redistribute the mass

335   emitted by vehicle sources in the vertical dimension, taking the very local physics influencing that vertical transport of fresh

336   emissions into account. We therefore focus on determining the at-source vertical transport of emitted mass associated with

337   VIT.

338   We start with the formulae for the transport of chemical species by vertical diffusion:

339
$$\frac{\partial c_i}{\partial t} = \frac{\partial}{\partial z}\left(K\frac{\partial c_i}{\partial z}\right) + E_i \tag{10}$$

340   Where c_i is the emitted chemical species, K represents the sum of all forms of thermal turbulent transfer in the grid-cell, and

341   E_i is the emissions source term for the species emitted at the surface (applied as a lower boundary condition on the diffusion

342   equation). For grid-cells containing roadways and hence mobile emissions, we split K into meteorological and vehicle-induced

343   components (K_T and K_{VIT} respectively), and the emissions into those from mobile sources and those from all other sources

344   ($E_{i,mob}$ and $E_{i,oth}$, respectively):

345
$$\frac{\partial c_i}{\partial t} = \frac{\partial}{\partial z}\left[(K_T + K_{VIT})\frac{\partial c_i}{\partial z}\right] + E_{i,mob} + E_{i,oth} \tag{11}$$

346   The terms in (11) may be rearranged:

347
$$\frac{\partial c_i}{\partial t} = \left\{\frac{\partial}{\partial z}\left[K_T\frac{\partial c_i}{\partial z}\right] + E_{i,oth}\right\} + \left\{\frac{\partial}{\partial z}\left[(K_T + K_{VIT})\frac{\partial c_i}{\partial z}\right] + E_{i,mob}\right\} - \left\{\frac{\partial}{\partial z}\left[K_T\frac{\partial c_i}{\partial z}\right]\right\} \tag{12}$$

348

349 The first bracketed term in (12) describes the rate of change of the chemical due to its emission by non-mobile area sources

350 and vertical diffusion due to meteorological sources of turbulence within the grid-cell, but outside of the sub-grid-scale

351 roadway. The second term describes the rate of change of the vertical diffusion of the mobile-source-emitted pollutants over

352 the sub-grid-cell roadway, which experiences both meteorological and roadway turbulence, and the final term prevents double-

353 counting of the meteorological component in equation (11), which is equivalent to equation (12). Note that turbulent mixing

354 for non-emitted chemicals is determined by solving equation (5), and for chemicals which are not emitted from mobile on-

355 road sources, equation (10) is solved, with $E_i = E_{i,oth}$. This form of the diffusion equation (12) allows the net change in

356 concentration to be calculated from three successive calls of the diffusion solver, starting from the same initial concentration

357 field. One advantage of this approach is that existing code modules for the solution of the vertical diffusion equation may be

358 used – rather than being used once, they are used three times, with different values for the input coefficients of thermal turbulent

359 transfer coefficient (K). The solution, once a suitable means of estimating K_{VIT} is available, is thus relatively easy to implement

360 in existing numerical air pollution model frameworks.

361 **2.6 Comparison of energy densities: VIT, Solar, and Urban Perturbations in Sensible and Latent Heat**

362 The relative contribution of TKE from VIT towards energy density can be compared to the daytime solar maximum energy

363 input to illustrate why VKT has relatively little impact during daylight hours, particularly in the summer. The maximum TKE

364 from VIT can be determined easily from Figure 3 and the use of our formulae; Figure 3(a) shows vehicle km travelled values

365 ranging from a maximum of 308 in the highest density 10km grid cell in North America (New York City) down through four

366 orders of magnitude in background grid cells with few vehicles. A typical urban value would be 30.8 VKT: this gives an F_c

367 value from our formulae of 3.08 vehicles s^{-1} for a 10km grid cell size. Assuming that the vehicles are all cars, from our

368 formulae we have a corresponding total TKE added at the point crossed by the vehicles, at height z=h_{cars}=1.5 m, of 7.48 m^2 s^{-2}.

369 We can combine this and the F_c value along with the area and volume of a lane of a roadway to estimate the energy density

370 (E_{VIT}) on dimensional grounds:

371
$$E_{VIT} = \left[\frac{(TKE)(air\ density)(lane\ volume)F_c}{(lane\ area)} \right] \tag{13}$$

372 Assuming each vehicle has a length of 4.5 m, width of 2.0 m, height of 1.5m, a lane length of 10 km, and an air density of

373 1.225 kg m^{-3}, one arrives at 84.8 kg s^{-3}, and values ranging from a North American grid maximum of 848 kg s^{-3} to a background

374 value four orders of magnitude smaller (8.48x10^{-2} kg s^{-3}). These energy densities may be compared to the typical solar energy

375 density reaching the surface at mid-latitudes of 1300 W m^{-2}, or in SI units, 1300 kg s^{-3}, and the typical range of perturbations

376 in latent and sensible heat fluxes associated with the use of a more complex urban radiative transfer scheme (the Town Energy

377 Balance module; Mason, 2000) in our 2.5km grid cell size simulations (typical diurnal ranges in the perturbations associated

378 with/without use of TEB: latent: -200 to +3 W m^{-2}; sensible: -100 to +100 W m^{-2} respectively). That is, under most daylight

379 conditions, the energy densities associated with VIT will be relatively small compared to the solar energy density at midday,

380 with a typical urban value of 6.5%, and range from 65% in the cell with the highest VKT values down to 0.0065% in
381 background conditions where the vehicle numbers are relatively small. Urban traffic however may contribute similar energy
382 levels as the changes in net latent and sensible heat fluxes associated with the use of an urban canopy radiative transfer model.
383 We also note that at night, during the low sun angle conditions of early dawn late evening, and during the lower sun angles of
384 winter, the relative importance of VIT to solar radiative input will be larger. Consequently, the impact of VIT will be higher
385 at night and in the early morning rush hour, and at other times when the sun is down or sun angles are low, as is demonstrated
386 below.

387 **2.7 GEM-MACH simulations**

388 A research version of the Global Environmental Multiscale – Modelling Air-quality and CHemistry (GEM-MACH) numerical
389 air quality model, based on version 2.0.3 of the GEM-MACH platform, was used for the simulations carried out here (Makar
390 *et al.*, 2017; Moran *et al.*, 2010; Moran *et al.*, 2018; Chen *et al.*, 2020). GEM-MACH is a comprehensive 3D deterministic
391 predictive numerical transport model, with process modules for gas and aqueous phase chemistry, inorganic particle
392 thermodynamics, secondary organic aerosol formation, vertical diffusion (in which area sources such as vehicle emissions are
393 treated as lower boundary conditions on the vertical diffusion equation), advective transport, and particle microphysics and
394 deposition. The model makes use of a sectional approach for the aerosol size distribution, here employing 12 aerosol bins.
395 The version used here also follows the "fully coupled" paradigm – the aerosols formed in the model's chemical modules in
396 turn may modify the model's meteorology via the direct and indirect effects (Makar *et al.*, 2015a,b; Makar *et al.*, 2017). The
397 meteorological model forming the basis of the simulations carried out here is version 4.9.8 of the Global Environmental
398 Multiscale weather forecast model (Cote *et al.*, 1998a,b; Caron *et al.*, 2015; Milbrandt *et al.*, 2016). Emissions for the
399 simulations conducted here were created from the most recent available inventories at the time the simulations were carried
400 out – the 2015 Canadian area and point source emissions inventory, 2013 Canadian transportation (onroad and offroad)
401 emissions inventory, and 2011-based projected 2017 US emissions inventory. As noted above, the model simulations were
402 carried out on two separate model domains shown in Figure 5; a 10 km horizontal grid cell size North American domain, and
403 a 2.5km horizontal grid cell size PanAm Games domain. For the 10km domain, simulations were for the month of July, 2016,
404 while for the higher resolution model, month-long summer (July 2015) and winter (January 2016) simulations were carried
405 out, with and without the VIT parameterization. These periods were based on the availability of emissions data, previous
406 model simulations for the same time periods appearing in the literature (Makar *et al.*, 2017; Stroud *et al.*, 2020), and the timing
407 of a prior field study (Stroud *et al.*, 2020).

408 **2.8 VIT as a Sub-grid-scale Phenomena**

409 It should be noted that the VIT enhancements to turbulent exchange coefficients are used to determine the vertical distribution
410 of freshly emitted pollutants at each model time step – they are not applied for all species within a model grid cell. Similar
411 sub-grid-scale approaches are used for the vertical redistribution of mass from large stack sources of pollutants, where

412 buoyancy calculations are applied to determine the rise and vertical distribution of pollutants from large industrial sources.
413 Both stacks and roadways are treated as sub-grid-scale sources of pollutants which are influenced by very local sources of
414 energy (stacks: high emission temperatures and exit velocities; roadways: vehicle induced turbulence) resulting in an enhanced
415 vertical redistribution of newly emitted chemical species. In both cases, the vertical transport results from an interplay between
416 the energy associated with the emission process (stacks: high temperature emissions with the ambient vertical temperature
417 profile; VIT: kinetic energy imparted to the atmosphere in which emissions have been injected with the ambient turbulent
418 kinetic energy). This interaction precludes a treatment solely from the standpoint of model input emissions, since the extent
419 of the mixing will depend on the local atmospheric conditions as well as the energy added due to the manner in which the
420 emissions occur. Both processes could be addressed by large eddy simulation modelling on a very local scale, but
421 parameterizations are required in both cases for regional scale simulations. In both cases, the parameterized vertical
422 redistribution of pollutants is applied to freshly emitted species – the horizontal spatial extent of the emitting region is
423 sufficiently small that although present, the enhanced mixing will have a minor effect on the redistribution of pre-existing
424 chemicals and on other atmospheric constituents affected by vertical transport. VIT in the context of regional chemical
425 transport models is thus best treated as a subgridscale phenomena applied to fresh emissions, in direct analogy to the approach
426 taken for large stack emissions.

427

3 Results

3.1 VIT Height Dependence as a Gaussian Distribution

430 Under Methods, we describe the potential for the use of a Gaussian distribution to describe the fall-off in TKE with height
431 above vehicles. Using the equations presented there, we have analyzed VIT studies appearing in the literature, determining
432 the decrease in TKE as a function of height from published figures, then fitting these data to a Gaussian distribution to the
433 height above ground. The result of this analysis for several data sets is shown in Table 1, generated by extracting vehicle
434 centerline TKE values from contour plots of published data, and is subdivided into isolated vehicle and vehicle ensemble
435 studies and cases.
436 The inferred mixing length shows a marked variation between that of isolated vehicles or the lead vehicle in an ensemble, and
437 that of other vehicles appearing further back in the ensemble. Both directly observed and CFD modelled values of the inferred
438 mixing length for *isolated* vehicles or the *lead* vehicles of an ensemble vary from 2.5 to 5.13 m. For subsequent vehicles in
439 an ensemble, the mixing lengths increase to range from 4.6 to 41m. The difference in mixing length between the lead vehicle
440 in an ensemble, and subsequent identical vehicles appearing later in the ensemble also increases. For example note that diesel
441 truck mixing lengths inferred from the CFD modelling examining different vehicle configurations (Kim *et al.*, 2016) increase
442 from 5.13 to 14.64 m, and the mixing lengths for automobiles increase from 2.50 m (isolated automobile), to 4.6m (automobile
443 two vehicles back from a lead diesel truck), to 9.41 m (automobile immediately behind a leading diesel truck). The mixing

444 length associated with VIT may also be significantly influenced by the ambient wind and local built environment – the mixing

445 length associated with the component of TKE due to VIT within street canyons (Woodward *et al.*, 2019; Zhang *et al.*, 2017)

446 ranges from 2/3 to greater than the street canyon height, with maximum mixing lengths of 41m. It is important to note that

447 these mixing lengths are driven by the vehicle passage within the canyon; they result from the additional TKE added

448 with/without vehicles in the CFD simulations. The above data show that a Gaussian distribution provides a reasonable

449 description of the decrease of TKE from vehicles with height, and, under realistic traffic conditions, the mixing lengths increase

450 in size, and are be considerably larger than those of isolated vehicles, and are comparable to or greater than the near-surface

451 vertical discretization of air quality models.

452 The length scales associated with VIT range from 2.50 m in the case of isolated vehicles (Kim *et al.*, 2016), through ~10 m

453 for vehicles moving in ensembles (Woodward *et al.*, 2019; Zhang *et al.*, 2017) up to 41 m, with the larger values being typical

454 for urban street canyons. The latter describe the specific regions VIT is expected to have the greatest impact, given the high

455 vehicle density within the urban core. However, our parameterization makes use of length scales derived from observations

456 on open (non-street canyon) freeways (Gordon *et al.* 2012; Miller *et al.*, 2018), and thus may underestimate the length scales

457 in the urban core. The impact of multiple vehicles travelling in an ensemble on open roadways was specifically depicted in

458 the open roadway simulations of Kim *et al.* (2016) reproduced in Methods (Figure 1), where the vertical extent of turbulent

459 mixing was shown to grow with increasing number of vehicles travelling in an ensemble. Furthermore, as was discussed and

460 demonstrated in Methods using the diffusivity equation, the length scale of the turbulence need not be greater than the model

461 lowest layer resolution in order to capture the impacts of VIT on mixing, being due in part to the gradient in turbulence with

462 height.

463 **3.2 Model Domains and Evaluation Data**

464 Our 3D air-quality model (GEM-MACH) and our VIT parameterization, including its diurnal variation, are described under

465 Methods. Two air-quality model grid cell size and domain configurations were used for our simulations – the first employs a

466 10km grid cell size with a North American domain, and is used for the current operational GEM-MACH air-quality forecast

467 (Moran *et al.*, 2010; Moran *et al.*, 2018; Figure 5(a)). The second was a 2.5km grid-cell resolution domain focused on the

468 region between southern Ontario, Quebec and northeastern USA (Joe *et al.*, 2018; Ren *et al.*, 2020; Stroud *et al.*, 2020; Figure

469 5(b)).

470 The impact of VIT was determined through paired model simulations, with and without the VIT parameterization, evaluated

471 against surface monitoring network data. The latter include hourly model output for ozone (O_3), nitrogen dioxide (NO_2), and

472 particulate matter with diameters less than 2.5 μm (PM2.5), across North America and in our high resolution eastern North

473 America domain, evaluated at observation station locations with data from the AirNow network (AirNow, 2020). Observation

474 station locations used in simulation evaluation for these species are shown in Figure 6, for the two model configurations. The

475 juxtaposition of observation stations with urban populations (where the highest vehicle density may be found) may be seen by

476 comparing Figure 6 with Figure S2.

3.3 Continental 10km Grid Cell Size Domain Evaluation

Simulations were carried out for the month of July, 2016 for the 10km grid cell size North American domain. Model performance metrics used to here (see Methods) are described in Table S1, and provided for the 10 km resolution "VIT" and "No VIT" simulations relative to the hourly observation data for PM2.5, NO_2, and O_3 in Table 2. These three chemicals were chosen due to their well-known link to human health impacts of air pollution (Steib *et al.*, 2008; Abelsohn *et al.*, 2011). The addition of VIT improved the scores for most performance metrics (bold-face print in Table 2). For NO_2, the addition of VIT improved all scores with the exception of the correlation coefficient, which was degraded in the third digit. All PM2.5 scores improved, with the exception of the mean bias, which became more negative by 0.5 μg m^{-3} across North America. All ozone scores improved, the exceptions being the correlation coefficient (which was the same for both simulations, or improved in the 3rd digit depending on the domain or country), and the ozone mean bias for the USA (which increased by +0.18 ppbv). Some of the improvements were substantial, when considered in a relative sense: this was most noticeable for the NO_2 scores, with the North American Mean Bias for NO_2 improving by a factor of 8.4, the mean gross error and index of agreement by 19%, the root mean square error by 25%, and the FAC2 score by 6%. Relative improvements for PM2.5 across North America were more modest (ranging from 0.3% for FAC2 to 14% for the correlation coefficient. The corresponding relative changes for O_3 ranged from a 22% reduction in the mean bias magnitude to a fraction of a percent improvement for FAC2, mean gross error, root mean square error, and index of agreement. Overall, the model performance for the Continental 10km domain July 2016 simulations improved across different metrics, indicating that the increased vertical turbulent mixing resulting from the incorporation of VIT results in a more accurate representation of atmospheric mixing and chemistry.

The timing and spatial distribution of the differences in the 29 day mean values of NO_2, PM2.5 and O_3 at 10 and 22 UT (6 AM and 6 PM EDT) are shown in Figure 7. NO_2 and PM2.5 have decreased in the urban areas and along the major road networks in the early morning (Figure 7(a,b)), while the ozone (Figure 7(c)) increases in the urban areas and along the roadways, with a minor increase in the surrounding countryside. The VIT effect occurs at night and in the early morning: the average differences are minimal by 6 PM EDT (Figure 7 (b,d,f)). This diurnal cycle of the average impact of VIT is expected: at night and during the early morning the radiative-transfer driven atmosphere is relatively stable, natural background turbulence is low in magnitude, and the relative contribution of VIT is therefore large. The reverse is true during the later morning to late afternoon, as the solar radiative balance causes near-surface turbulence to rise several orders of magnitude relative to nighttime values, and the relative contribution of VIT at those times becomes minimal. The strongest contribution of VIT thus occurs under more stable atmospheric conditions: at night and in the early morning.

The all-domain model performance metrics of Table 2 were also calculated for each measurement station, and the appropriate differences in the metrics or their absolute values were used to determine location-specific impacts of the VIT parameterization for NO_2, PM2.5 and O_3 (Figures 8, S3 and S4). Differences in the values of the metrics between the two simulations are shown, with the sign of the differences arranged so that red/blue colours indicate better performance for the VIT/No VIT simulations respectively, red indicating better scores for the VIT simulation. The colour scales in these Figures are arranged

510 to include 3 orders of magnitude between lowest and highest difference scores and zero, and to encompass the maximum value

511 of the differences observed at across all stations. The values vary between metrics and the chemical species, with the largest

512 changes occurring for NO_2, followed by PM2.5 and the smallest changes for O_3, relative to typical concentrations of these

513 species, and in accord with Table 2. NO_2 performance improvements with the VIT simulation (red colours) occur across most

514 stations for the FAC2, MGE, RMSE, COA and IOA scores (Figure 8(a,c,e,f,g)), while r and |MB| scores are more variable,

515 with some stations having better performance for the No VIT simulation. PM2.5 performance improvements are more mixed,

516 with large improvements for correlation coefficient (Figure S3(d)) and IOA (Figure S3(g), a mild but overall positive effect of

517 VIT for MGE, RMSE and COE (Figure S3(c,e,f)), and more stations showing a degradation of performance for FAC2 and

518 |MB|, echoing the net effect for these last two metrics seen in Table 2. O_3 performance shows a strong regional variation

519 (Figure S4): most scores improve with the use of the VIT parameterization in the western and north-eastern parts of the

520 continent, and degrade in the south-eastern USA. The degradation in the south-eastern (e.g. increases in O_3 concentrations in

521 a region which already experiences a positive O_3 bias) are associated with the transport of urban O_3 precursors into forested

522 areas in the region, with additional O_3 production occurring there. These effects may be removed through the introduction of

523 an additional parameterization for the reduced turbulence and shading within forested canopies (Makar *et al.*, 2017; Figure

524 S5), with the combined parameterizations resulting in improvements in both NO_2 and O_3 performance. While the use of VIT

525 degrades O_3 performance in this region, this degradation is thus very small relative to the large improvements noted with the

526 canopy effect (see Makar *et al.*, 2017; Fig S5 and its associated discussion in the S.I.). Another significant feature is the

527 improvement (red colours) in most O_3 station scores in urban regions (Figure S4). These improved scores largely result from

528 increases in ozone in the early morning hours (Figure 7(e)), where VIT has resulted in increased vertical mixing, reducing

529 surface level NO_x and hence NO_x titration of ozone, and also by mixing higher ozone levels aloft down into the lowest model

530 layer.

531 Overall, the impact of the VIT parameterization was to improve North American simulation accuracy, across multiple

532 statistical metrics, with the most significant improvements in the model performance for simulated NO_2. Spatially, model

533 performance was generally greatest in urban regions and western and northeastern North America, though this depends on the

534 chemical species and the performance metric chosen.

535 **3.7 Eastern North America 2.5km Grid Cell Size Domain Evaluation**

536 With the use of a smaller grid cell size (i.e. "higher resolution"), meteorological models and on-line air-quality models such

537 as GEM-MACH have the option of employing theoretical approaches which better simulate the more complex radiative

538 transfer and physical environment-induced turbulence of urban areas. Urban heat islands are known to have a significant effect

539 on turbulence, for example (Mason, 2000; Makar *et al.*, 2006). In these simulations, we make use of the Town Energy Balance

540 (TEB; Mason, 2000; Leroyer *et al.*, 2014; Lemonsu *et al.*, 2005), a single-layer urban canopy module which solves the

541 equations for urban atmosphere's surface and energy budgets for a variety of urban elements (roads, walls, roofs), then

542 aggregates the results for the net urban canopy. Such parameterizations are inappropriate for use in larger grid cell size models

543   due to the latter's inability to resolve individual surface types and spatial gradients at the city scale. An important consideration
544   in determining the relative importance of vehicle-induced turbulence is whether improvements in performance still occur,
545   when these other sources of turbulent kinetic energy are included explicitly. We address this issue in our 2.5km grid cell size
546   modelling by employing the TEB parameterization, for both VIT and No VIT simulations, evaluating both simulations against
547   surface monitoring network observations as before. Both summer and winter simulations were carried out on the blue domain
548   of Figure 5(b), and the same performance metrics were calculated as for the larger North American simulations (Table 3).

549   A similar pattern of performance improvement can be seen between 10km and 2.5km grid cell sized, comparing Tables 2 and
550   3, with improvements due to the use of VIT predominating in both summer and winter: despite the addition of a more explicit
551   urban radiative balance approach, better scores were achieved with the addition of the VIT parameterization. Note that
552   comparisons between the 2.5km and 10km simulations for similar emissions inputs appear elsewhere in the literature (Stroud
553   *et al.*, 2020). The number of improved scores increases from summer to winter. Stable atmospheric conditions and low
554   meteorological turbulence levels are more common in winter than summer, during both day and night, and the impact of the
555   additional source of turbulence is thus proportionally stronger in the winter season. The VIT effects at the urban scale are the
556   strongest for NO_2 and PM2.5, and less noticeable for simulated O_3, similar to the North American domain simulation. The
557   largest improvements for the three species and across seasons occur for winter PM2.5, with the improved performance taking
558   place in the first or second digit of the given metric. Metric differences for NO_2 aside from mean bias occur in the second to
559   third digit in the winter, with summer differences occurring in the first to 2nd digit. Changes to O_3 are relatively minor, with
560   some improvements and degradation in performance in the 3rd digits across the different metrics.

561   UT-hour average differences between the two 2.5km grid-cell size simulations, for the three species evaluated for the summer
562   and winter simulations, appear in Figures (S6, S7), and Figures (9, 10) respectively. The summer differences in surface
563   concentration (Figure S6) are the largest at 6 AM local time (10UT; first column of panels), and have largely decreased to near
564   zero by 6 PM (22 UT; last column). Corresponding concentration vertical distribution differences along a cross-section linking
565   the major cities show the early morning depletion (increase) of NO_2, PM2.5 (O_3) are coupled to increases (decreases) aloft
566   (Figure S7, first column of panels). NO_2 and PM2.5 reductions extend to altitudes of up to 2km with the increase in radiative-
567   driven turbulence during the day, while the change in NOx/VOC regime aloft leads to increases in lower Troposphere O_3
568   (Figure S7, second column). Daytime mixing increases lead to a reduction in the effect by nightfall (Figure S7, third column).
569   VIT-enhanced transport of NO_2 from urban to rural areas can also be seen (Figure S6, center column/first column; note
570   increases in NO_2 on the periphery of the urban areas, pink to red colours). This additional NO_x added to NO_x-limited regions
571   leads to low-level (mostly sub-ppbv) increases in daytime O_3 at 10AM which persist through to 6PM. Over the Great Lakes,
572   the change in vertical transport on land, coupled with daytime lake breeze circulation (Makar *et al.*, 2010; Joe *et al.*, 2018;
573   Stroud *et al.*, 2020) results in a decrease in daytime NO_2 and PM2.5 over the Lakes and corresponding late-afternoon O_3
574   increases (Figure S6, blue colours in centre column of panels over the lakes for NO_2 and PM2.5, red colours in the final panel
575   of the sequence for O_3). The changes in the near-roadway environment thus have larger regional effects, changing the pathway
576   and reaction chemistry of transported chemicals on a regional scale.

577 The stronger impact of VIT under winter conditions is illustrated in Figures 9 and 10; NO$_2$ decreases (Figures 9,10 (a,b,c))

578 persist throughout the day, though to a lower degree by 6 PM (contrast Figures S6,S7 (a,b,c) to Figures 9,10(a,b,c)). The

579 vertical influence of VIT reaches an altitude of approximately 2 km in the winter (1 km in the summer); contrast Figure S7

580 and Figure 10. The absence of winter biogenic hydrocarbon production during the day has likely limited the daytime increase

581 in O$_3$ to the cities (compare Figure S6(h) with Figure 9(h)). The large effect of VIT along major roadways can be seen in

582 both Figures S6 and 9, particularly in the 6AM column of panels (a,d,g) in both figures, with the greatest reductions aside from

583 urban regions occurring along major roadways (e.g. Chicago to Detroit area).

584 Differences in station-specific performance scores for the two simulations for the 2.5km grid-cell size domain, constructed as

585 for the 10km domain, are shown in Figures S8, S9, and S10 (summer) and Figures S11, S12 and S13 (winter) for NO$_2$, PM2.5

586 and O$_3$, respectively.

587 The summer scores (Figs. S8, S9, S11) show the most significant improvements in the urban areas across all performance

588 metrics, with the largest relative magnitude differences for NO$_2$ and PM2.5, and lower magnitude changes for O$_3$. As for the

589 North American simulations, O$_3$ performance improvements occur in the cities, due to increased vertical mixing, and, O$_3$ scores

590 in rural regions have degraded, but may be improved with the use of a forest canopy parameterization, as discussed further in

591 the SI (Figure S10, S13, S5). The overall impact of the incorporation of the VIT parameterization is clearly a positive one,

592 particularly in urban areas: VIT has been shown to have a significant impact on summertime urban and suburban scale

593 photochemistry.

594 The metrics of the winter 2.5km station-specific evaluation for NO$_2$ (Figure S11) show both local improvements and

595 degradation in performance, depending on location. Wintertime PM2.5 performance improves across most metrics and most

596 locations (Figure S12). Wintertime ozone performance is variable, though improvements can be seen for most metrics within

597 the largest urban areas (Figure S13).

598 **4 Discussion and Conclusions**

599 Our work implies that the turbulence associated with vehicle motion is capable of having a significant effect on the

600 concentrations of key pollutants in the lower atmosphere. Incorporating that effect into both continental-scale and higher

601 resolution regional/urban scale air implementations of a pollution model resulted in an overall improvement in model

602 performance, across several different performance metrics. The improvement at higher resolution (when the TEB urban

603 parameterization was included in the model setup) implies that the mixing associated with urban radiative transfer and

604 roughness is not sufficient to account for the observed pollutant concentrations; the effect of VIT is robust despite differences

605 in radiative transfer schemes and across different horizontal resolutions.

606 However, we also acknowledge several limitations of our VIT formulation and have recommendations for future work which

607 would allow it to be improved and the uncertainties in our analysis reduced.

608 First, we have assumed that single-vehicle induced turbulence accounts for all of the turbulent kinetic energy contributed by
609 vehicles (Gordon *et al.*, 2012; Miller *et al.*, 2018). The passage of multiple vehicles also induces a "wake flow" in their
610 direction of motion. While this effect has been recognized in very high resolution roadway-scale models (Eskridge and
611 Catalano, 1987; Eskridge *et al.*, 1991), the breakdown of opposing wake flows into turbulence (arising from two-way traffic
612 and/or multiple lanes of traffic travelling at different speeds) has not been examined, to the best of our knowledge. However,
613 these wake flows are of sufficiently high energy that their residual power is being harnessed via vertical-turbine wind power
614 generation systems in both Turkey (Devecitech, 2020) and Scotland (Shell, 2020). The single-vehicle additive
615 parameterization we have created here may thus underestimate the net turbulent effect of vehicle passage. At the same time,
616 our assumption that individual VIT within a grid cell is simply additive may also be incorrect, resulting in overestimates of
617 that portion of the net VIT. With the advent of Doppler LIDAR systems with sufficient time resolution to capture turbulence,
618 we advocate for and are currently embarking on new observation studies employing these systems in scan mode across
619 highways, to fully characterize all vehicle-induced contributions to turbulence as a function of the number and type of vehicles
620 crossing below a LIDAR scan path perpendicular to the highway.

621 Second, our assumption that each vehicle's pathway crosses the grid cell is a considerable source of uncertainty. There we are
622 limited by the lack of availability of simultaneous vehicle speed and number data. However, recent developments in satellite-
623 based radar technology have been shown to provide accurate estimates of the speed of individual vehicles along major
624 highways (Meyer *et al.*, 2006; Bethke *et al.*, 2006), and binning and collection of these data may improve the linkage between
625 the more commonly available vehicle-km-travelled data and VIT beyond that used here. Other sources of gridded vehicle
626 and/or road density data (World Bank, 2018) should also be explored.

627 Third, one consideration for our parameterization is the issue of "traffic jams"; a large number of vehicles being present on the
628 road without much motion in such conditions. However, we note that in this case, the number of vehicles crossing a point in
629 space will drop – that is, if the underlying traffic data (vehicle-km-travelled) is of sufficient quality that traffic jams are
630 included, the existing parameterization should adequately handle these effects. Both our second and this third consideration
631 argue for the creation of more accurate vehicle travel data for use in air-quality models.

632 Last, we note that the ambient concentrations of pollutants such as NO_2, O_3 and PM2.5 are influenced by a host of factors
633 included in other parameterizations of air-quality models, and in the quality of the available emissions data. However, we
634 have shown here that improvements in the forecast quality of three different species with human-health impacts may be
635 achieved through the same process improvement. An examination of all of the other possible sources of error in air-quality
636 models is beyond the scope of this work. We also emphasize that the work does not identify a deficiency in existing
637 meteorological boundary layer turbulence models. Rather, that the at-source vertical transport of fresh pollutants from the
638 mobile sector needs to take into account local sources of energy for transport at the point of emission (whether in large stacks
639 (Gordon *et al.*, 2018; Akingunola *et al.*, 2018) or over roadways (as examined here)).

640 Despite the uncertainties identified above, our analysis has shown:

641 (1)   The drop-off of VIT with height above moving vehicles is well-represented by a Gaussian distribution, from multiple
642 measurement and computational fluid dynamics modelling studies.

643 (2)   The mixing lengths inferred from these studies ranges from 2.50 m (for individual isolated cars) through ~10 m
644 (vehicle ensembles) to 41 m (vehicle ensembles in a street canyon environment). We also note that the gradient in the net
645 thermal turbulent transfer coefficients drives concentration changes due to VIT. The expectation that VIT is capable of vertical
646 transport out of the lowest layers of a regional model is therefore a reasonable one.

647 (3)   The magnitude of the localized energy input from VIT, while smaller than the input of solar energy during daylight
648 hours, is equivalent in magnitude to the energy perturbations resulting from the use of a state-of-the-art urban radiative balance
649 model (TEB; see Methods). That is, locally, VIT has sufficient energy to be equivalent to the impact of an improved urban
650 radiative transfer scheme – underlining its importance for vertical transport of pollutants.

651 (4)   The impact of VIT depends on both local traffic conditions and the background meteorological conditions, with the
652 maximum effect occurring when turbulence in the ambient atmosphere is relatively weak (night through early morning), and
653 traffic levels are relatively high (morning rush hour).

654 (5)   The use of the VIT parameterization has been demonstrated to result in decreases in air-quality model error, across
655 three different key pollutants, with the most striking results for mean biases, without resorting to the use of imposed minima
656 in the thermal turbulent exchange coefficients frequently used in air-quality models.

657 (6)   VIT has a significant impact on the rapid vertical distribution of freshly emitted pollutants on the very localized scale
658 of roadways where the enhanced mixing occurs, in analogy to the rapid vertical transport used in parameterizations of plume
659 rise from large stacks. Its impact on mixing of pre-existing meteorological and chemical variables on the grid-cell scale is
660 expected to be small.

661 Based on these findings, we conclude that VIT has a significant impact on pollutant transport and dispersion out of the lowest
662 layer of the atmosphere, and recommend its inclusion in air-quality models. Further improvements to the parameterizations
663 found herein would result from additional observations of TKE using Doppler lidar techniques, of vehicle ensembles under
664 realistic driving conditions.

665 **Acknowledgments**

666

667 The authors would like to acknowledge the contract assistance of Elisa Boutzis under the direction of J. Zhang in the generation
668 of VKT gridded fields.

669

670 **References**

671

672 Abelsohn, A., and Steib, D.M., Health effects of outdoor air pollution: approach to counseling patients
673   using the Air Quality Health Index, Can. Fam. Phys., 57, 881-887, 2011.
674 Adelman, Z., Baek, B.H. , Brandmeyer, J., Seppanen, C., Naess, B., and Yang, D., Spatial Surrogate
675   Development for 2014 Emissions Modeling Platforms, *2017 International Emissions Inventory*
676   *Conference,*   Aug.   14-18,   Baltimore,   MD,   USA,   2017   (see
677   https://www.epa.gov/sites/production/files/2017-11/documents/surrogate_developement.pdf).
678 AirNow, 2020: https://www.airnow.gov/, last accessed February 21, 2020.
679 Akingunola, A., Makar, P.A., Zhang, J., Darlington, A., Li, S.-M., Gordon, M., Moran, M.D., Zheng, Q.,
680   A chemical transport model study of plume-rise and particle size distribution for the Athabasca oil
681   sands, Atmos. Chem. Phys., 18, 8667-8688, 2018.
682 Bou-Zeid, E., Meneveau, C., Parlange, M.B., Large-eddy simulation of neutral atmospheric boundary
683   layer flow over heterogeneous surfaces: Blending height and effective surface roughness, Water
684   Resources Research, 40, W02505, doi:10.1029/2003WR02475, 2004.
685 Bethke, K.-H., Baumgartner, S., Gabele, M., Hounam, D., Kemptner, E., Klement, E., Krieger, G., and
686   Erxleben, R., Air- and spaceborne monitoring of road traffic using SAR moving target indication –
687   Project TRAMRAD, ISPRS J. Phot. Remote Sens., 61, 243-259, 2006.
688 Bradshaw, P., Possible origin of Prandt's mixing-length theory, Nature, 249,   135–136.
689   Bibcode:1974Natur.249..135B. doi:10.1038/249135b0, 1974.
690 Briggs, G.A.: Plume rise predictions, Lectures on air Pollution and environmental impact analyses. In:
691   Workshop Proceedings, Sept. 29-Oct. 3, pp. 59-111, *American Meteorological Society*, Boston, MA,
692   USA., 1975.
693 Briggs, G.A.: Plume rise and buoyancy effects, atmospheric sciences and power production. In:
694   Randerson, D. (Ed.), DOE/TIC-27601 (DE84005177), TN. Technical Information Center, U.S. Dept.
695   of Energy, Oak Ridge, USA,.pp 327-366, 1984.
696 Caron, J-F., Milewski, T., Buehner, M., Fillion, L., Reszka, M., Macpherson, S., St-James, J.,
697   Implementation of deterministic weather forecasting systems based on ensemble-variational data
698   assimilation at Environment Canada. Part II: The regional system. Mon. Wea. Rev. 143: 2560– 2580,
699   doi:10.1175/MWR-D-14-00353.1, 2015.
700 Chen, J. and GEM-MACH development team, GEM-MACH atmospheric chemistry module for the GEM
701   numerical weather pre-diction model, Environment and Climate Change Canada, Zenodo,
702   https://doi.org/10.5281/zenodo.2579386, 2019, last accessed March 3, 2020.
703 Cote, J.C., Gravel, S., Methot, A., Patoine, A., Roch, M., Staniforth, A., The operational CMC-MRB
704   Global Environmental Multiscale (GEM) Model. Part I: design considerations and formulation, Mon.
705   Wea. Rev., 126, 1373-1395, 1998(a).

706 Cote, J.C., Desmarais, J.-G., Gravel, G., Methot, A., Patoine, A., The operational CMC- MRB Global

707   Environmental Multiscale (GEM) Model. Part II: results. Mon. Wea. Rev., 126, 1397-1418, 1998(b).

708 Devecitech, 2020: https://devecitech.com/?page_id=5, last accessed February 21, 2020.

709 Di Sabatino S., Kastner-Klein, P., Berkowicz, R., Britter, R.E., and Fedorovich, E., The modeling of

710   turbulence from traffic in urban dispersion models – Part I: Theoretical considerations. Environmental

711   Fluid Mechanics, 3, 129-143, 2003.

712 EPA, 2017: Data available from US EPA:

713 ftp://newftp.epa.gov/air/emismod/2011/v3platform/2017emissions/2017ek_cb6v2_v6_11g_inputs_onro

714   ad.zip, last accessed March 3, 2020.

715 Eskridge, R.E., and Catalano, J.A., ROADWAY – a numerical model for predicting air pollutants near

716   highways, Users Guide, US EPA, 134pp, 1987 (also available at

717   https://nepis.epa.gov/Exe/ZyPDF.cgi/20015RHA.PDF?Dockey=20015RHA.PDF, last accessed

718   February 25, 2020).

719 Eskridge, R.E., Petersen, W.B., and Rao, S.T., Turbulent diffusion behind vehicles: effect of traffic speed

720   on pollutant concentrations, J. Air & Waste Management Ass., 41:3, 312-317, 1991. DOI:

721   10.1080/10473289.1991.10466848

722 Galmarini, S., Hogrefe, C., Brunner, D., Makar, P.A., Baklanov, A., Preface, Atm. Env., 115, 340-344,

723   2015.

724 Gordon, M., Makar, P.A., Staebler, R.M., Zhang, J., Akingunola, A., Gong, W., and Li, S.-M., A

725   comparison of plume rise algorithms to stack plume measurements in the Athabasca Oil Sands,

726   Atmos. Chem. Phys., 18, 14695-14714, 2018.

727 Gordon, M., Staebler, R.M., Liggio, J., Makar, P.A., Li, S.-M., Wentzell, J., Lu, G., Lee, P., and Brook,

728   J.R., Measurements of enhanced turbulent mixing near highways, J. App. Met & Clim., 51, 1618-

729   1632, 2012.

730 Hu, X.-M., Klein, P.M., and Xue, M., Evaluation of the updated YSU Planetary Boundary Layer Scheme

731   within WRF for Wind Resource and Air Quality Assessments. J. Geophys. Res. Atmos., 118, 10,490–

732   10,505, doi:10.1002/jgrd.50823, 2013.

733 Joe, P., Belair, S., Ber Nier, N.B., Bouchet, V., Brook, J.R., Brunet, D., Burrows, W., Charland, J.-P.,

734   Dehghan, A., Driedger, N., Duhamie, C., Evans, G., Filion, A.-B., Frenette, R., DeGrandpre, J.,

735   Gultepe, I., Henderson, D., Herdt, A., Hilker, N., Huang, L., Hung, E., Isaac, G., Jeong, C.-H.,

736   Johnston, D., Klassen, J., Leroyer, S., Lin, H., MacDonald, M., MacPhee, J., Mariani, Z., Munoz, T.,

737   Ried, J., Robichaud, A., Rochon, Y., Shairsing, K., Sills, D., Spacek, L., Stroud, C., Su, Y., Taylor,

738   N., Vanos, J., Voogt, J., Wang, J.M., Wiechers, T., Wren, S., Yang, H., Yip, T., The Environment

739   Canada Pan and ParaPan American science showcase project, Bull. Am. Met. Soc., 921-953, 2018.

Kain, J.S., The Kain-Fritsch convective parameterization: an update, J. App. Met., 43, 170-181, 2004.

Kastner-Klein P., Fedorovich, E., Ketzel, M., Berkowicz, R., and Britter, R., The modelling of turbulence from traffic in urban dispersion models – Part II: Evaluation against laboratory and fullscale concentration measurements in street canyons. Environmental Fluid Mechanics, 3, 145-172, 2003.

Kim, Y., Huang, L., Gong, S., Jia, C.Q., A new approach to quantifying vehicle induced turbulence for complex traffic scenarios, C. J. Chem. Eng., 24, 71-78, 2016.

Kim, Y., Sartelet, K., Raut, J-C., Chazette, P., Influence of an urban canopy model and PBL schemes on vertical mixing for air quality modeling over Greater Paris, Atm. Env., 107, 289-306, 2015.

Kim, Y., Quantification of vehicle-induced turbulence on roadways using computational fluid dynamics simulation, M.Sc. Thesis, Department of Chemical Engineering and Applied Chemistry, University of Toronto, 93 pp., 2011.

Klein, P.M., Hu, X.-M., and Xue, M., Impacts of mixing processes in the nocturnal atmospheric boundary layer on urban ozone concentrations. Boundary Layer Meteorology, 150, 107-130, 2014.

Lemonsu, A., Belair, S., Mailhot, J., Leroyer, S., Evaluation of the Town Energy Balance model in cold and snowy conditions during the Montreal urban snow experiment, 2005, J. App. Met. Clim., 49, 346-362, 2010.

Leroyer, S., Belair, S., Husain, S.Z., and Mailhot, J., Subkilometer numerical weather prediction in an urban coastal area: a case study over the Vancouver metropolitan area, J. App. Met. Clim., 53, 1433-1453, 2014.

Makar, P.A., Staebler, R.M., Akingunola, A., Zhang, J., McLinden, C., Kharol, S.K., Pabla, B., Cheung, P. and Zheng, Q., The effects of forest canopy shading and turbulence on boundary layer ozone, Nature Communications, 8, art. no. 15243, doi: 10.1038/ncomms15243, 2017.

Makar, P.A., Gong, W., Milbrandt, J., Hogrefe, C., Zhang, Y., Curci, G., Zabkar, R., Im, U., Balzarini, A., Baro, R., Bianconi, R., Cheung, P., Forkel, R., Gravel, S., Hirtl, H., Honzak, L., Hou, A., Jimenz-Guerrero, P., Langer, M., Moran, M.D., Pabla, B., Perez, J.L., Pirovano,G., San Jose,R., Tuccella, P., Werhahn, J., Zhang, J., Galmarini, S., Feedbacks between air pollution and weather, part 1: Effects on weather. Atm. Env., 115, 442-469, 2015a.

Makar, P.A., Gong, W., Hogrefe, C., Zhang, Y., Curci, G., Zabkar, R., Milbrandt, J., Im, U., Balzarini, A., Baro, R., Bianconi, R., Cheung, P., Forkel, R., Gravel, S., Hirtl, H., Honzak, L., Hou, A., Jimenz-Guerrero, P., Langer, M., Moran, M.D., Pabla, B., Perez, J.L., Pirovano,G., San Jose,R., Tuccella, P., Werhahn, J., Zhang, J., Galmarini, S., Feedbacks between air pollution and weather, part 2: Effects on chemistry. Atm. Env., 115, 499-526, 2015b.

772 Makar, P.A., Nissen, R., Teakles, A., Zhang, J., Zheng, Q., Moran, M.D., Yau, H., diCenzo, C., Turbulent
773   transport, emissions and the role of compensating errors in chemical transport models, Geo. Mod.
774   Dev., 7, 1001-1024, 2014.

775 Makar, P.A., Zhang, J., Gong, W., Stroud, C., Sills, D., Hayden, K.L., Brook, J., Levy, I., Mihele, C.,
776   Moran, M.D., Tarasick, D.W., He, H., and Plummer, D., Mass tracking for chemical analysis: the
777   causes of ozone formation in southern Ontario during BAQS-Met 2007, Atmos. Chem. Phys., 10,
778   11151-11173, 2010.

779 Makar, P.A., *et al.*, Anthropogenic heat flux, urban properties, and regional weather, Atm. Env. 40, 2750-
780   2766, 2006.

781 Mason, V., A physically-based scheme for the urban energy balance in atmospheric models, Bound. Lay.
782   Met., 94, 357-397, 2000.

783 Mensink, C., Lefebre, F., Janssen, L., and Cornelis, J., A comparison of three street canyon models with
784   measurements at an urban station in Antwerp, Belgium, Env. Mod. Soft., 21, 514-516, 2014.

785 Meyer, F., Hinz, S., Laika, A., Weihing, D., Bamler, R., Performance analysis of the TerraSAR-X Traffic
786   monitoring concept, ISPRS J. Phot. Remote Sens., 61, 225-242, 2006.

787 Milbrandt, J.A., Bélair, S., Faucher, M., Vallée, M., Carrera, M.L., and Glazer, A., The pan-Canadian
788   High Resolution (2.5 km) Deterministic Prediction System, Weather and Forecasting, 31 (6), pp.
789   1791-1816, 2016.

790 Miller, S.J., Gordon, M., Staebler, R.M., and Taylor, P.A., A study of the spatial variation of vehicle-
791   induced turbulence on highways using measurements from a mobile platform, Bound. Lay. Met.,
792   https://doi.org/10.1007/s10546-018-0416-9, 29 pp., 2018.

793 Moran, M.D., Lupu, A., Zhang, J., Savic-Jovcic, V., Gravel, S., A comprehensive performance evaluation
794   of the next generation of the Canadian operational regional air quality deterministic prediction system,
795   Springer Proceedings in Complexity, pp 75-81, 2018.

796 Moran M.D., S. Ménard, D. Talbot, P. Huang, P.A. Makar, W. Gong, H. Landry, S. Gravel, S. Gong, L-
797   P. Crevier, A. Kallaur, M. Sassi, Particulate-matter forecasting with GEM-MACH15, a new Canadian
798   air-quality forecast model. In: Steyn DG, Rao ST (eds) Air Pollution Modelling and Its Application
799   XX, Springer, Dordrecht, 289-292, 2010.

800 Prandtl, L., Z. angew, Math. Mech. 5 (1): 136–139, 1925.

801 Rao, K.S., Gunter, R.L., White, J.R., and Hosker, R.P., Turbulence and dispersion modeling near
802   highways, Atm. Env., 36, 4337-4346, 2002.

803 Rao, S.T., Sedefian, L., and Czapksi, U.H., Characteristics of turbulence and dispersion of pollutants near
804   major highways, J. App. Met., 18, 286-293, 1979.

805   Ren, S., Stroud, C., Belair, S., Leroyer, S., Moran, M., Zhang, J., Akingunola, A., and Makar, P., Impact
806   of Urban Land Use and Anthropogenic Heat on Air Quality in Urban Environments, Springer
807   Proceedings in Complexity, pp. 153-158, 2020.

808   Shell, 2020: https://www.shell.com/inside-energy/turbine-turns-traffic-into-energy.html, last accessed
809   February 21, 2020.

810   Stieb, D.M., Burnett, R.T., Smith-Doiron, M., Brion, O., Hwashin, H.S., and Economou, V., A new
811   multipollutant, no-threshold air quality health index based on short-term associations observed in
812   daily time-series analyses, J. Air W. Man. Ass., 58, 435-450, 2008.

813   Stroud, C., Ren, S., Zhang, J., Moran, M., Akingunola, A., Makar, P.A., Munoz-Alpizar, R., Leroyer, S.,
814   Bélair, S., Sills, D., Brook, J.R., Chemical analysis of surface-level ozone exceedances during the
815   2015 pan American games, Atmosphere, 11 (6), art. no. 572, 2020.

816   Taylor, B., National Pollution Release Inventory, Environment and Climate Change Canada, personal
817   communication, 2019.

818   Woodward, H., Stettler, M., Pavlidis, D., Aristodemou, E., ApSimon, H., and Pain, C.., A large eddy
819   simulation of the dispersion of traffic emissions by moving vehicles at an intersection, Atmospheric
820   Environment, 215, 116891, 2019.

821   World Bank, 2018: https://datacatalog.worldbank.org/dataset/grip-global-roads-inventory-dataset-2018-
822   road-density, last accessed February 21, 2020.

823   Zhang, Y., Gu, Z., and Yu, C.W., Large eddy simulation of vehicle induced turbulence in an urban street
824   canyon with a new dynamically vehicle-tracking scheme, Aerosol and Air Quality Research, 17, 865-
825   874, doi: 10.4209/aaqr.2016.05.0204, 2017.

826

827

828
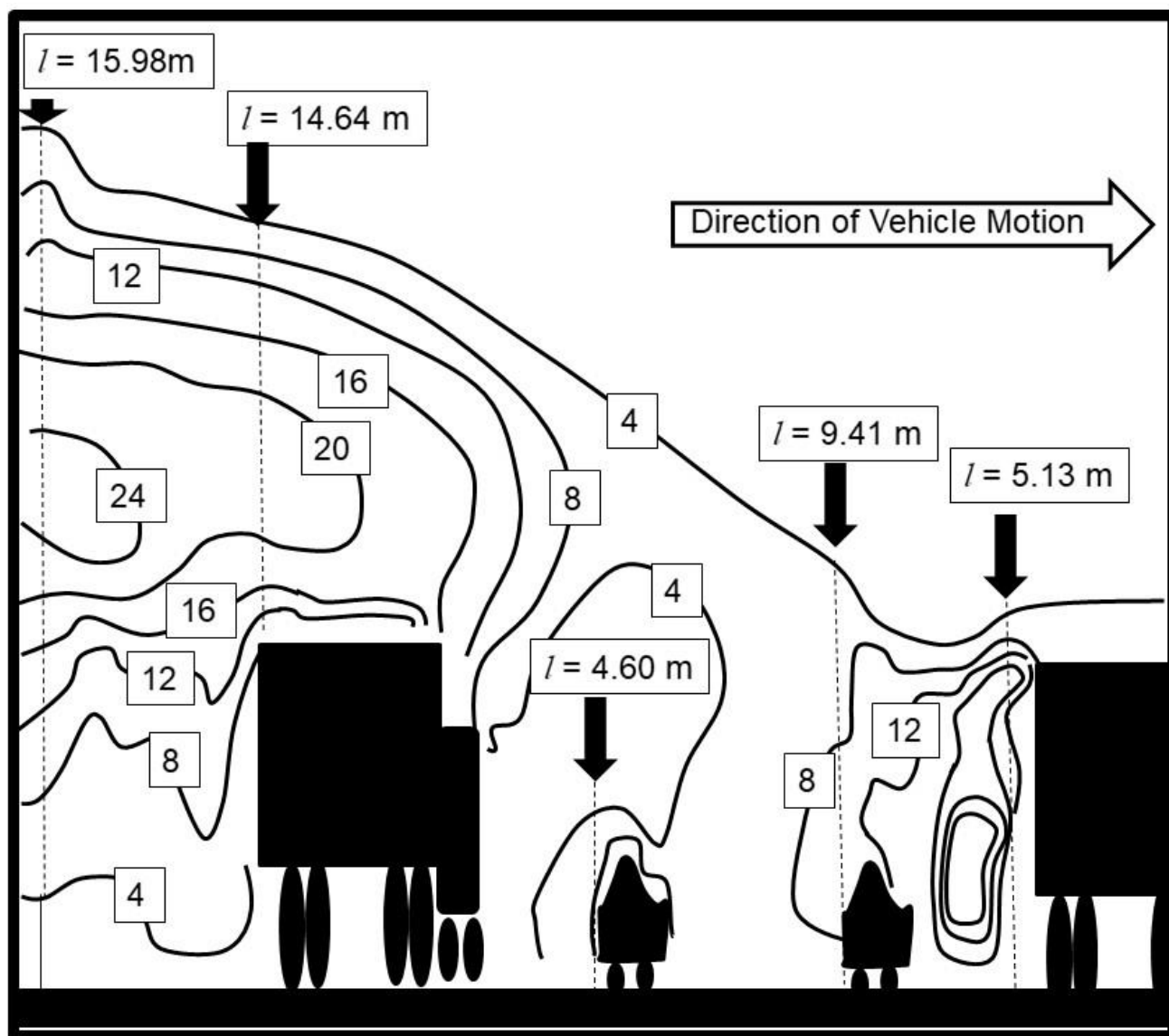
Figure 1. Example of length scales associated with an ensemble of vehicles (after Kim *et al*., 2016, Figure 14). TKE contours along dashed lines were extracted and fit to equations (1,2) for Table 1. Note that the length scale of turbulence immediately behind the leading vehicle, a large transport truck is only 3m, while the length scale immediately behind the trailing vehicle in the ensemble (an identical transport truck) is 12.73m.
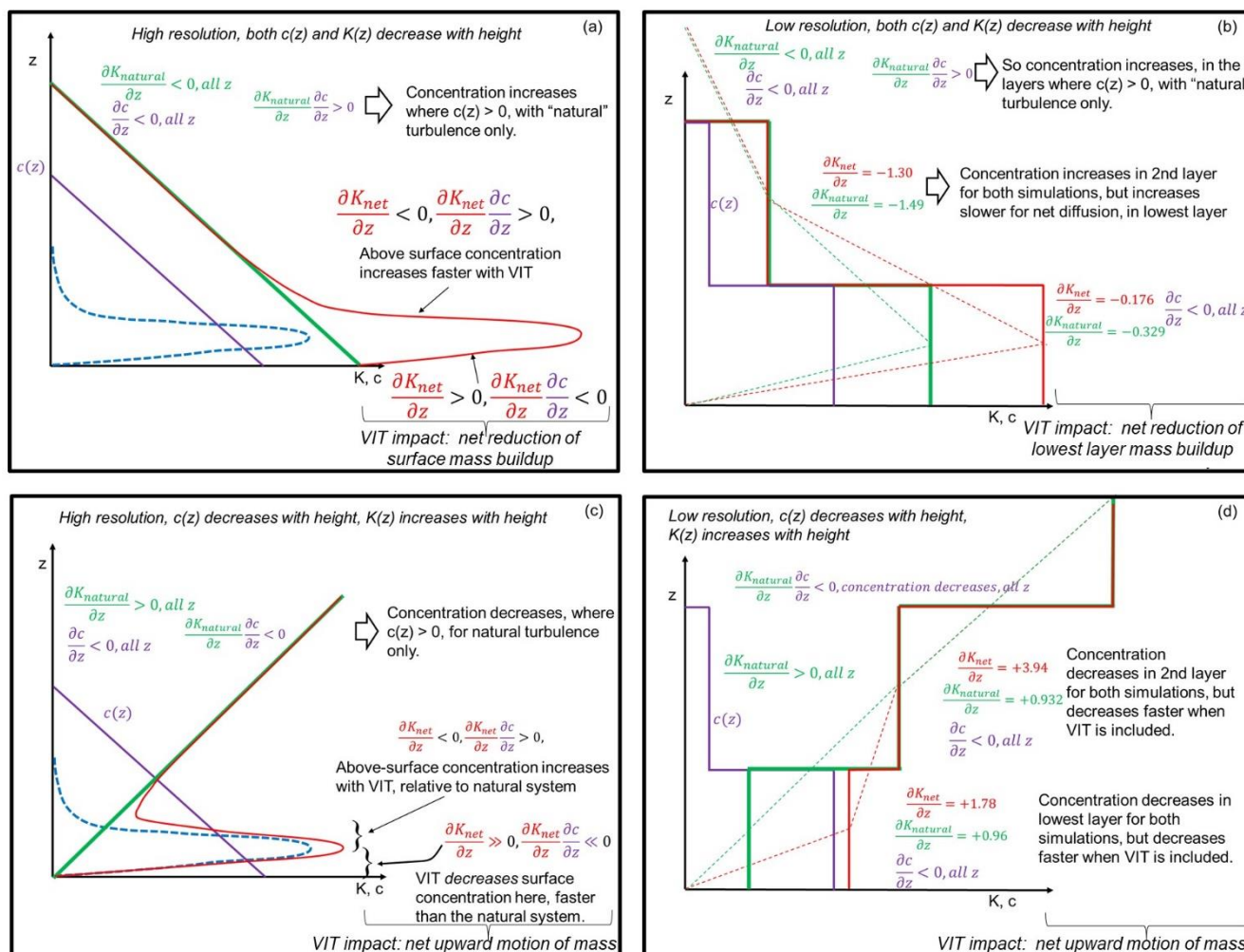
Figure 2. Illustration of the impact of VIT on the local vertical gradient of the thermal turbulent transfer coefficients, at low (a,c) and high (c,d) resolution. Purple, green, dashed blue, and red lines illustrate the height variation of concentration, meteorological or natural coefficient of thermal turbulent transfer, VIT coefficient of thermal turbulent transfer, and net coefficient of thermal turbulent transfer, respectively. (a,b) High and low resolution profiles and gradients, for the case where both concentration and meteorological thermal turbulent transfer coefficients decrease with height. (c,d) High and low resolution profiles and gradients, for the case where concentration decreases and meteorological thermal turbulent transfer coefficients increases with height.

842
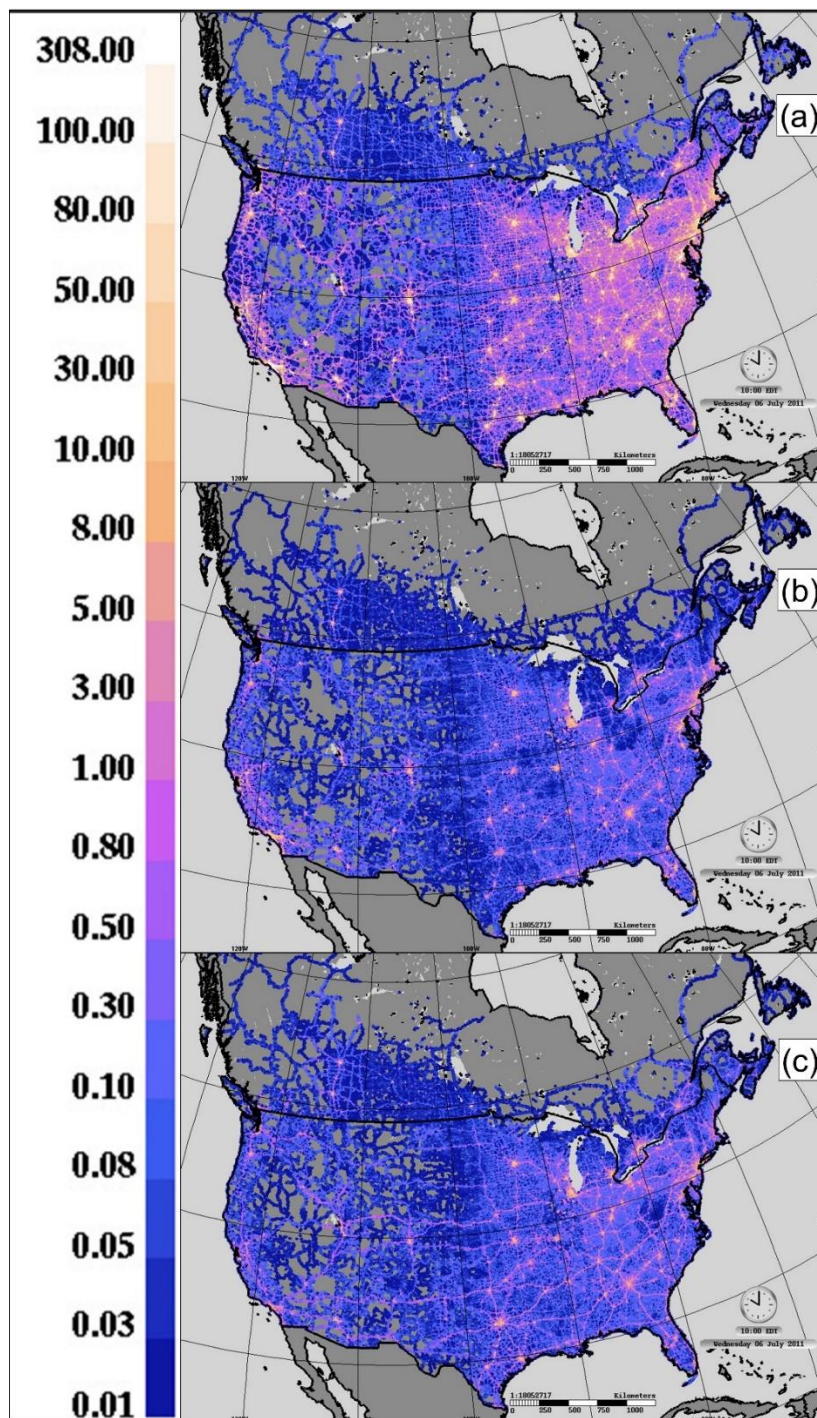
Figure 3. Vehicle km travelled per 10 km grid cell (km s^{-1}) for (a) cars, (b) mid-size vehicles and (c) trucks, July, 2015.

844
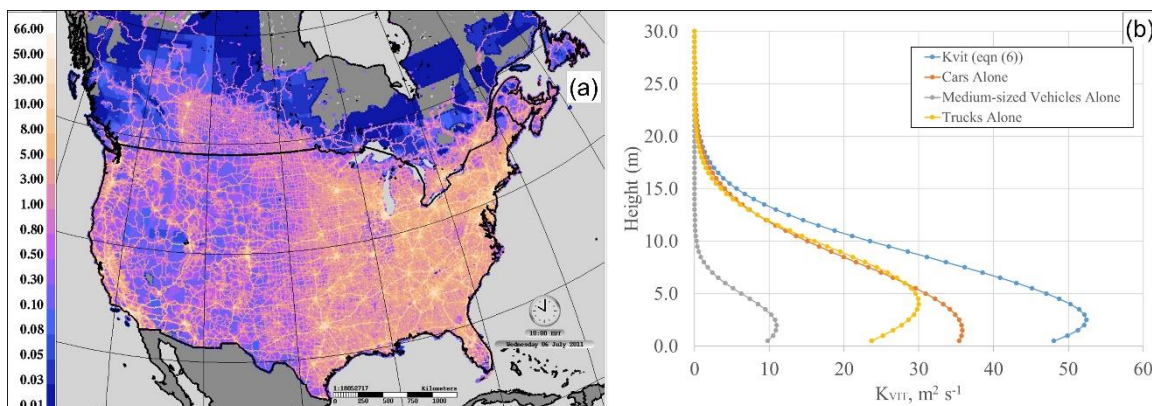
845

846   **Figure 4.** (a) Example estimated thermal turbulent transfer coefficients from VIT at 2 m elevation during a weekday at 10 am in July (m^{2}s^{-1}
847   ), using the VKT data of Figure 3. (b) Vertical profile of VIT thermal turbulent transfer coefficients at one meter resolution in central
848   Manhattan Island, and individual values for the TKE associated with cars, mid-sized vehicles and trucks considered separately, generated
849   using equation (8). Note that the profiles of (b) would be added to the ambient thermal diffusivity coefficients (see section 2.5, and
850   equation (12)).

851
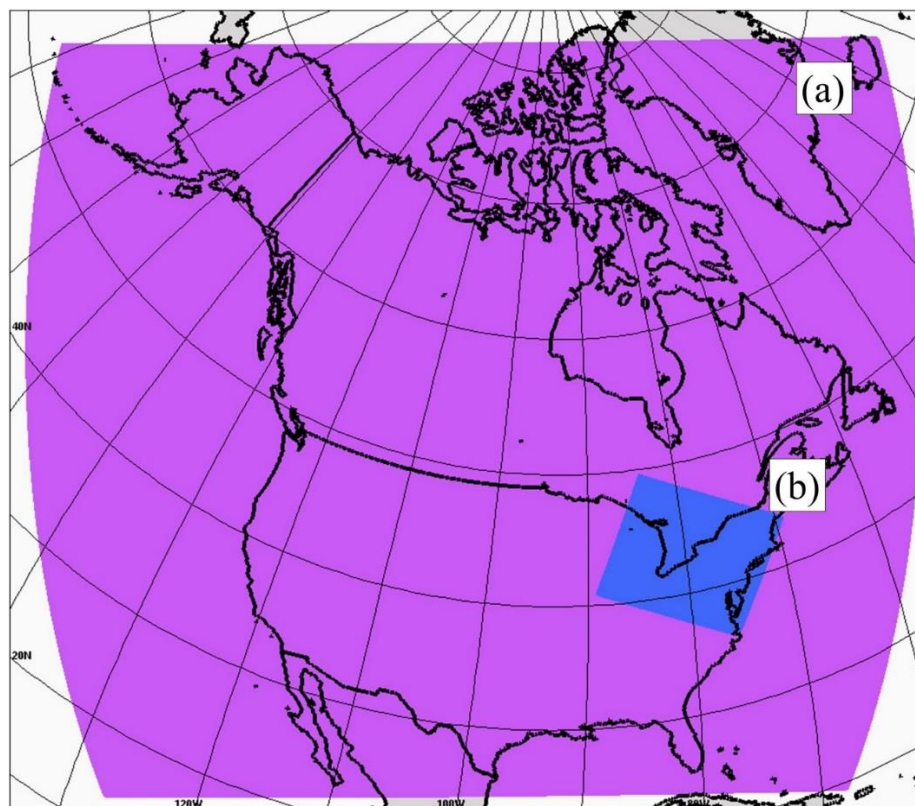
852

853   **Figure 5.** GEM-MACH test domains: (a) 10km grid cell size North American domain. (b) 2.5km grid cell size Pan Am domain.

854
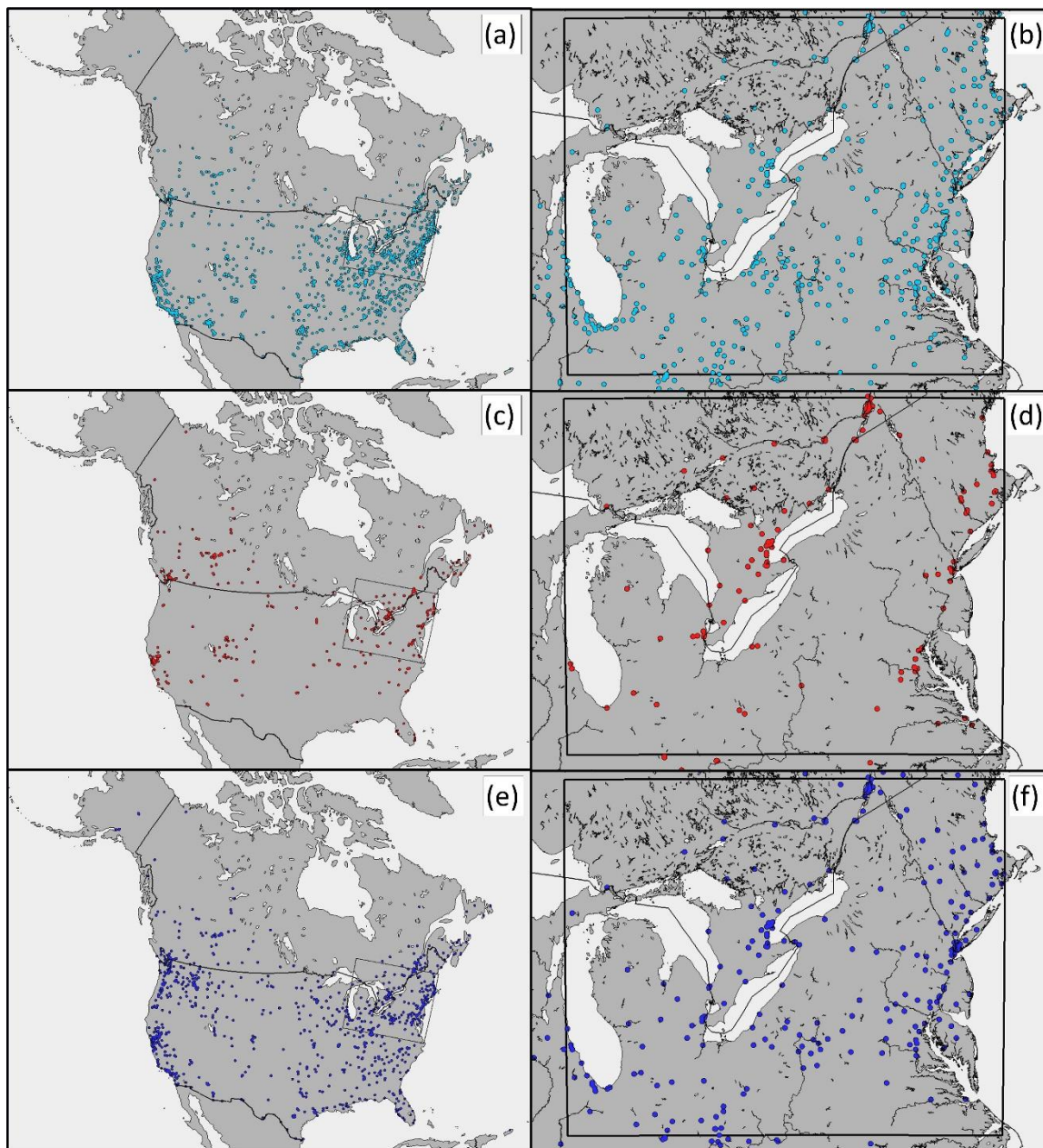
855
856 **Figure 6**. AIRNOW hourly observation station locations for ozone (a,b), nitrogen dioxide (c,d), and particulate matter with diameters less
857 than 2.5 μm (e,f). (a,c,e): Stations used for the 10km grid cell size domain evaluation. (b,d,f): Stations used for the 2.5km grid cell size
858 domain evaluation (all stations located within central box).

859
860
861
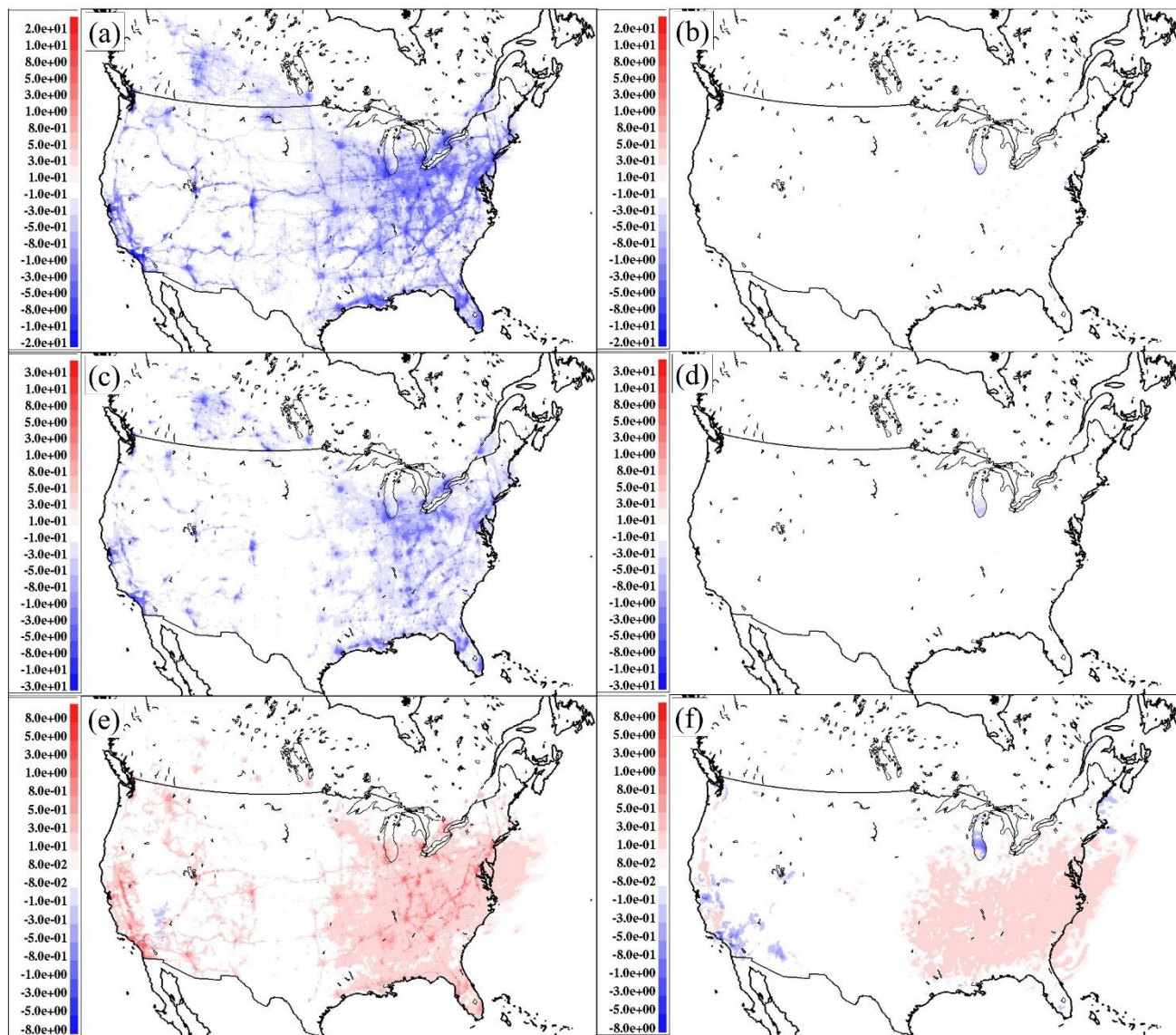
Figure 7. Difference in 29 day average NO$_2$, PM2.5 and O$_3$, July 2016 Continental 10km domain simulations (VIT simulation – No VIT simulation). Averages are paired at (a,c,e: 10UT, b,d,f: 22UT) according to species; (a,b): ΔNO$_2$(ppbv); (c,d) ΔPM2.5(μg m^{-3}); (e,f) ΔO$_3$(ppbv).
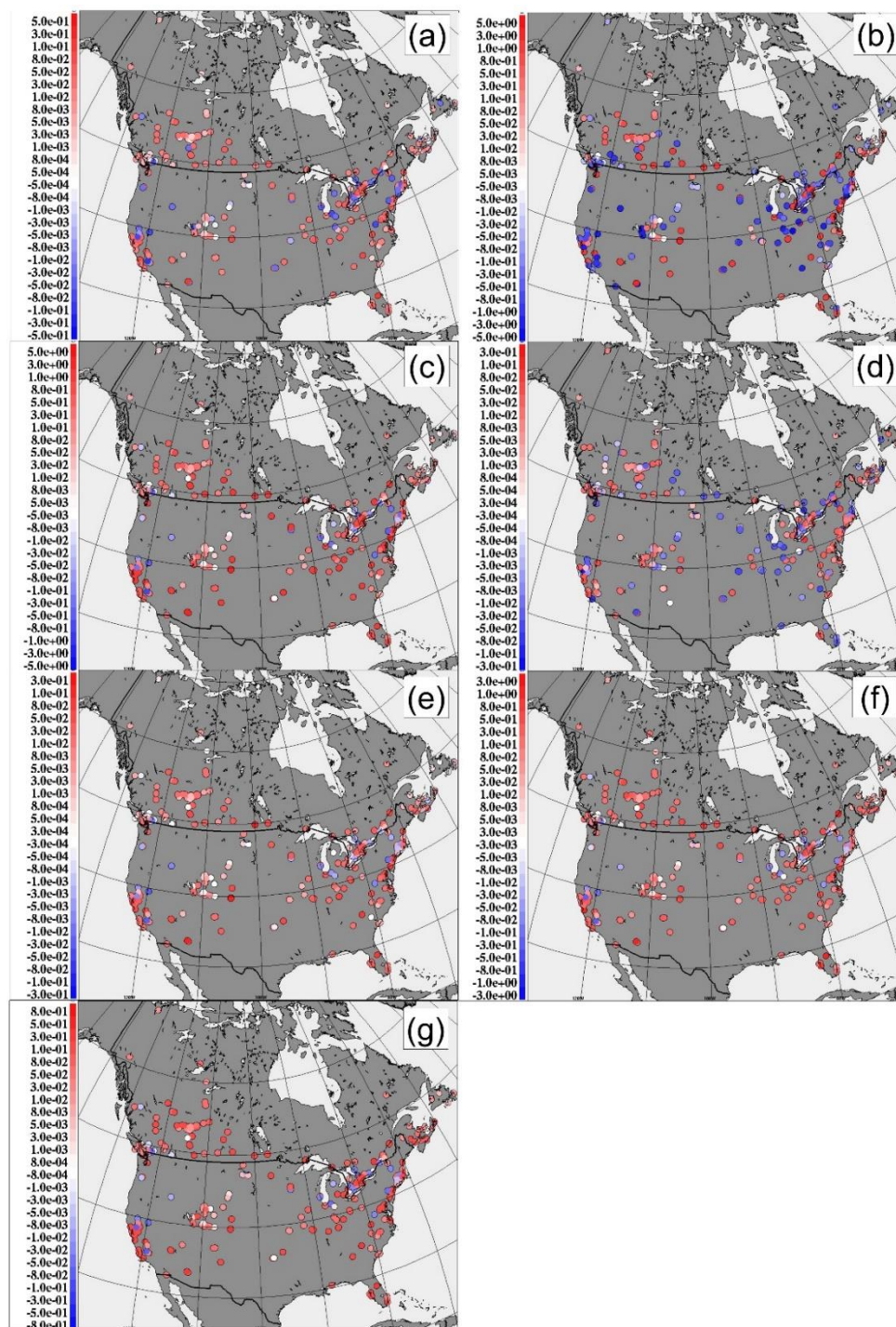
Figure 8. Change in model NO_2 performance at 358 North American surface monitoring sites, July 2016 (ppbv). Red colours indicate stations where the addition of the VIT parameterization improved model performance, blue colours indicate stations where the addition of the VIT parameterization degraded model performance. (a) $\Delta FAC2_{VIT-No\,VIT}$; (b) $\Delta|MB|_{No\,VIT-VIT}$; (c) $\Delta MGE_{No\,VIT-VIT}$; (d) $\Delta r_{VIT-No\,VIT}$; (e) $\Delta RMSE_{No\,VIT-VIT}$; (f) $\Delta COE_{VIT-No\,VIT}$; (g) $\Delta IOA_{VIT-No\,VIT}$.

873

874
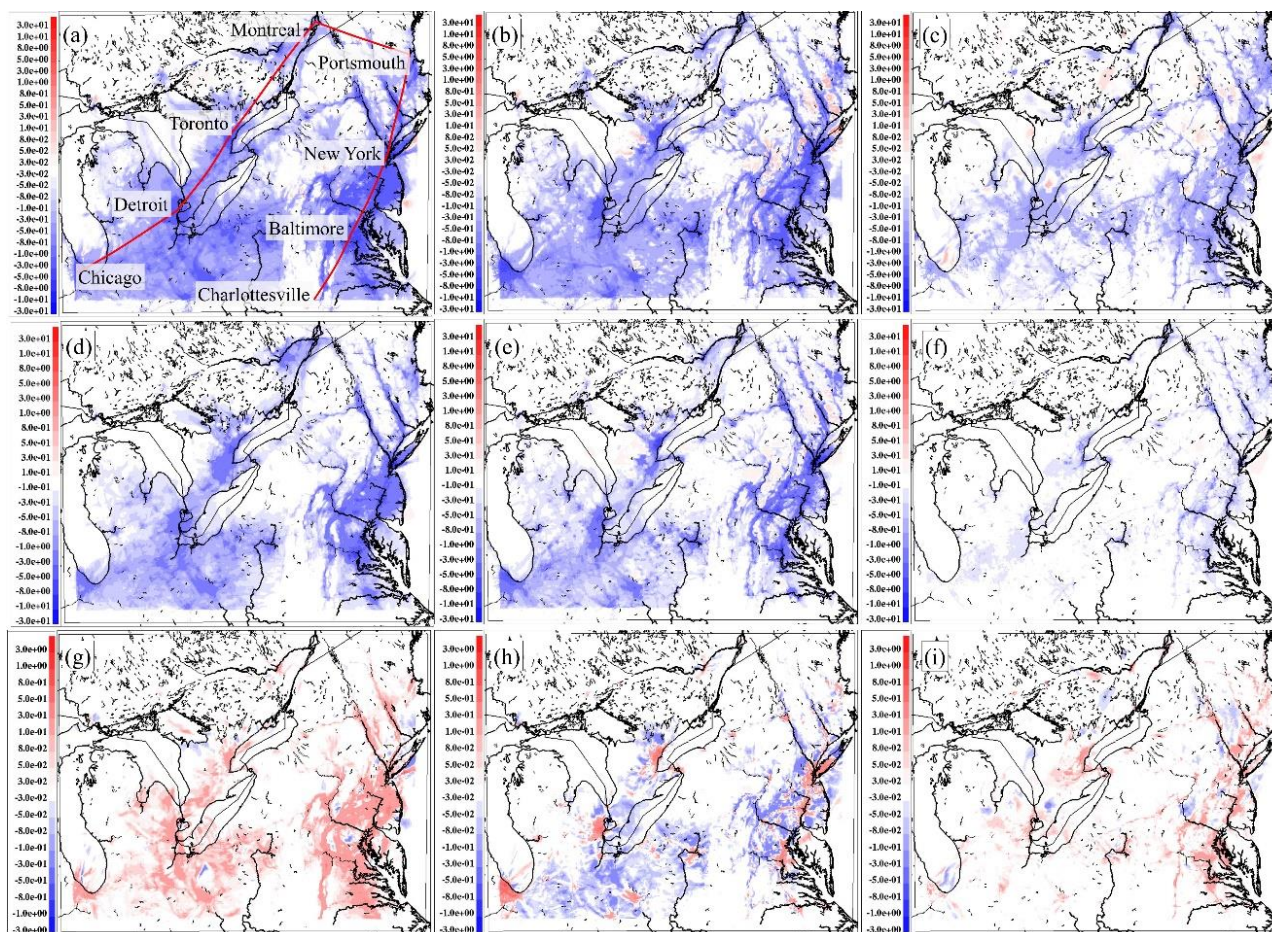
Figure 9. Difference in 30 day average surface NO₂, PM2.5 and O₃, January 2016, PanAm 2.5km grid cell size domain simulation. Averages are paired at (10, 14, and 22UT) according to species; (a,b,c): ΔNO_2;(ppbv) (d,e,f) $\Delta PM2.5$ (µg m⁻³); (g,h,i) ΔO_3 (ppbv). Red line in panel (a) indicates position of vertical cross-section shown in Figure 10.

879

880

881

882
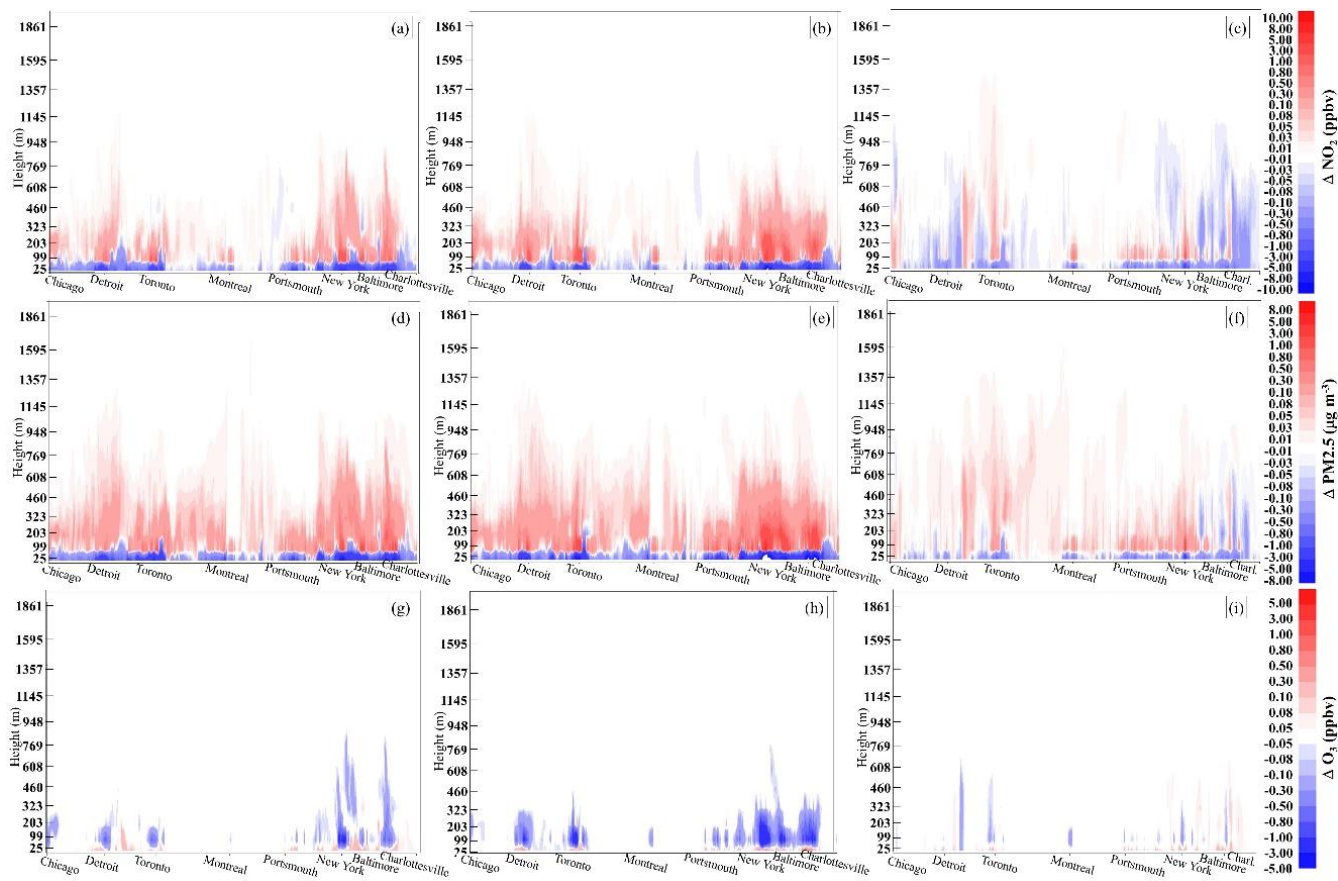
Figure 10. Vertical cross-sections of concentration differences between major eastern North American cities, January 2016, panels arranged as in Figure 9. Vertical coordinate: unitless hybrid, top-of-scale is approximately 2 km.

885

886
887 **Table 1.** Gaussian distribution fits of VIT TKE drop-off with height, from observation and CFD studies.

Study, Case	Slope	Intercept	R^2	Mixing length (z at $e^{\left(-\frac{(z-h_q)^2}{2\,\sigma_q^2}\right)} = 0.01$), m
Isolated vehicles:				
Rao *et al.* (2002), cube van, 50 mph, h_q = 2m	2.2452	1.8534	0.9856	3.53
Rao *et al.* (2002), cube van, 30 mph, h_q=2m	1.0230	1.4969	0.9709	4.22
Kim *et al.* (2016), lead automobile, h_q = 1.5m	4.6431	3.9013	0.8845	2.50
Kim *et al.* (2016), lead diesel cargo truck, h_q =4m	3.6143	4.2223	0.9355	5.13
Vehicle Ensembles:				
Kim *et al.* (2016), automobile immediately following lead diesel cargo truck, h_q = 1.5m	0.073529	4.1144	0.9801	9.41
Kim *et al* (2016), 2nd automobile, following lead diesel cargo truck, h_q = 1.5m	0.47337	3.9275	1.00[a]	4.60
Kim *et al.* (2016) 2nd diesel cargo truck, h_q = 4m	0.04070	4.7935	0.5424	14.64
Woodward *et al.* (2019) vehicle ensemble[b], h_q=1.5m, parallel to flow, right lane	0.01916	-1.2402	0.9135	17.01
Woodward *et al.* (2019) vehicle ensemble[b], h_q = 1.5m, parallel to flow, left lane	0.01155	-1.4532	0.7543	21.46
Woodward *et al.* (2019) vehicle ensemble[b], h_q = 1.5m, transverse to flow, right lane	0.012489	-1.4766	0.9667	20.70
Woodward *et al.* (2019) vehicle ensemble[b], h_q = 1.5m, transverse to flow, left lane	0.0098094	-1.7815	0.9536	23.16
Zhang *et al.* (2017), VS1: h_q = 1.6m, vehicle speed = 9 km hr^{-1}, Wind 11 km hr^{-1}	0.0029165	5.1706	0.6614	41.24
Zhang *et al.* (2017), VS2: h_q = 1.6m, speed = 36 km hr^{-1}, Wind 11 km hr^{-1}	0.005158	5.0964	0.8306	31.38
Zhang *et al.* (2017), VS3: h_q = 1.6m, vehicle speed = 36 km hr^{-1}, Wind 36 km hr^{-1}	0.007298	6.3394	0.9006	26.62
Zhang *et al.* (2017), VS4: h_q = 1.6m, vehicle speed = 36 km hr^{-1}, Wind 36 km hr^{-1}	0.005411	5.6387	0.9339	30.67
Zhang *et al.* (2017), VS5: h_q = 1.6m, vehicle speed = 36 km hr^{-1}, Wind 54 km hr^{-1}	0.003478	4.3150	0.8574	37.89

888
889   a.   Note that only two contour lines were available for retrieving TKE and height values from this vehicle within Figure 14 of Kim
890   et al. (2016); while the correlation coefficient is formally unity, this is a two-point line.
891   b.   Woodward et al. (2019) Figure 21 turbulent velocity components in the parallel and transverse directions were squared, and
892   distances were scaled to give equivalent distances from wind-tunnel to ambient environment.
893
894

veryhighhttps://doi.org/10.5194/acp-2020-1243

Table 2. Model performance for NO₂, PM2.5, and O₃, 10km grid cell size North American domain. No VIT refers to simulation without vehicle-induced turbulence, VIT refers to the simulation incorporating vehicle-induced turbulence. **Bold-face** print identifies the better score, italics the worse score, and regular font indicates similar performance, between the two simulations, for each metric and chemical species compared.

Species	Evaluation Metric	North America		Canada		USA	
		No VIT	VIT	No VIT	VIT	No VIT	VIT
NO₂ (ppbv)	FAC2	*0.449*	**0.474**	*0.437*	**0.464**	*0.461*	**0.484**
	MB	*1.195*	**0.142**	*1.553*	**0.716**	*0.860*	**-0.396**
	MGE	*4.226*	**3.542**	*3.679*	**3.057**	*4.738*	**3.996**
	NMGE	*0.832*	**0.698**	*0.911*	**0.757**	*0.783*	**0.661**
	r	**0.515**	*0.511*	**0.520**	*0.518*	**0.507**	*0.506*
	RMSE	*7.089*	**5.665**	*6.058*	**4.764**	*7.934*	**6.396**
	COE	*-0.083*	**0.092**	*-0.238*	**-0.029**	*-0.017*	**0.142**
	IOA	*0.459*	**0.546**	*0.381*	**0.486**	*0.492*	**0.571**
PM2.5 (µg m⁻³)	FAC2	*0.451*	**0.453**	*0.402*	**0.412**	**0.466**	*0.465*
	MB	**-2.116**	*-2.619*	**-0.032**	*-0.669*	**-2.688**	*-3.154*
	MGE	*4.982*	**4.733**	*4.733*	**4.237**	*5.043*	**4.864**
	NMGE	*0.672*	**0.638**	*0.879*	**0.787**	*0.632*	**0.610**
	r	*0.185*	**0.211**	*0.147*	**0.163**	*0.217*	**0.241**
	RMSE	*7.933*	**7.300**	*8.870*	**7.323**	*7.628*	**7.271**
	COE	*-0.203*	**-0.143**	*-0.431*	**-0.281**	*-0.188*	**-0.146**
	IOA	*0.399*	**0.429**	*0.285*	**0.360**	*0.406*	**0.427**
O₃ (ppbv)	FAC2	*0.819*	**0.823**	*0.760*	**0.767**	*0.830*	**0.833**
	MB	*-0.097*	**0.080**	*-3.652*	**-3.498**	**0.503**	*0.684*
	MGE	*10.050*	**10.009**	*8.111*	**8.023**	*10.379*	**10.346**
	NMGE	*0.325*	**0.323**	*0.343*	**0.339**	*0.322*	**0.321**
	r	0.707	0.707	*0.703*	**0.705**	0.694	0.694
	RMSE	*13.095*	**13.035**	*10.357*	**10.242**	*13.511*	**13.458**
	COE	*0.239*	**0.242**	*0.144*	**0.153**	*0.229*	**0.232**
	IOA	*0.619*	**0.621**	*0.572*	**0.577**	*0.615*	**0.616**

901 **Table 3.** Model performance for NO_2, PM2.5, and O_3, 2.5 km grid cell size Pan Am domain. No VIT refers to simulation without vehicle-
902 induced turbulence, VIT refers to the simulation incorporating vehicle-induced turbulence. **Bold-face** print identifies the better score, italics
903 the worse score, and regular font indicates similar performance, between the two simulations, for each metric and chemical species compared.

Species	Evaluation Metric	PanAm Domain July		PanAm Domain January	
		No VIT	VIT	No VIT	VIT
NO₂ (ppbv)	FAC2	*0.584*	**0.593**	**0.714**	*0.711*
	MB	*1.005*	**0.386**	*0.852*	**-0.328**
	MGE	*4.137*	**3.866**	*5.166*	**5.146**
	NMGE	*0.670*	**0.626**	*0.457*	**0.455**
	r	**0.560**	*0.543*	**0.736**	*0.693*
	RMSE	*6.909*	**6.373**	*7.917*	**7.892**
	COE	*0.059*	**0.121**	*0.348*	**0.350**
	IOA	*0.530*	**0.560**	*0.674*	**0.675**
PM2.5 (μg m⁻³)	FAC2	**0.573**	*0.569*	*0.563*	**0.592**
	MB	**-2.669**	*-3.055*	*3.930*	**2.362**
	MGE	*5.813*	**5.729**	*8.315*	**7.012**
	NMGE	*0.537*	**0.529**	*0.865*	**0.729**
	r	*0.338*	**0.346**	*0.163*	**0.170**
	RMSE	*8.972*	**8.791**	*24.875*	**23.194**
	COE	*-0.077*	**-0.061**	*-0.463*	**-0.234**
	IOA	*0.462*	**0.467**	*0.269*	**0.383**
O₃ (ppbv)	FAC2	*0.831*	**0.832**	*0.852*	**0.854**
	MB	**4.138**	*4.213*	**1.652**	*1.731*
	MGE	**10.640**	*10.648*	*6.433*	**6.427**
	NMGE	0.333	0.333	0.259	0.259
	r	0.709	0.709	**0.688**	*0.687*
	RMSE	**13.826**	*13.838*	*8.440*	**8.427**
	COE	0.146	0.146	*0.190*	**0.191**
	IOA	0.573	0.573	*0.595*	**0.596**

904
905